AGU PUBLICATIONS

JGR

Journal of Geophysical Research: Oceans

RESEARCH ARTICLE

10.1002/2016JC012519

Downstream evolution of the Kuroshio's time-varying transport and velocity structure

M. Andres[1], V. Mensah[2], S. Jan[2], M.-H. Chang[2], Y.-J. Yang[2], C. M. Lee[3], B. Ma[3], and T. B. Sanford[3]

[1]Physical Oceanography Department, Woods Hole Oceanographic Institution, Woods Hole, Massachusetts, USA, [2]Institute of Oceanography, National Taiwan University, Taipei, Taiwan, [3]Applied Physics Laboratory, University of Washington, Seattle, Washington, USA

Key Points:
- Kuroshio mean transport increases by 50% between Luzon and Taiwan, primarily via a downstream increase in thickness of the poleward flow
- Observations suggest a deep cyclonic recirculation east of Taiwan, which arises because the mean poleward flow impinges on the Ilan Ridge
- Transport and velocity structure east of Taiwan are modulated by arrivals of deep-reaching eddies and their interactions with the ridges

Correspondence to:
M. Andres,
mandres@whoi.edu

Citation:
Andres, M., V. Mensah, S. Jan, M.-H. Chang, Y.-J. Yang, C. M. Lee, B. Ma, and T. B. Sanford (2017), Downstream evolution of the Kuroshio's time-varying transport and velocity structure, *J. Geophys. Res. Oceans*, *122*, 3519–3542, doi:10.1002/2016JC012519.

Received 28 OCT 2016
Accepted 6 MAR 2017
Accepted article online 11 MAR 2017
Published online 2 MAY 2017

Abstract Observations from two companion field programs—Origins of the Kuroshio and Mindanao Current (OKMC) and Observations of Kuroshio Transport Variability (OKTV)—are used here to examine the Kuroshio's temporal and spatial evolution. Kuroshio strength and velocity structure were measured between June 2012 and November 2014 with pressure-sensor equipped inverted echo sounders (PIESs) and upward-looking acoustic Doppler current profilers (ADCPs) deployed across the current northeast of Luzon, Philippines, and east of Taiwan with an 8 month overlap in the two arrays' deployment periods. The time-mean net (i.e., integrated from the surface to the bottom) absolute transport increases downstream from 7.3 Sv (±4.4 Sv standard error) northeast of Luzon to 13.7 Sv (±3.6 Sv) east of Taiwan. The observed downstream increase is consistent with the return flow predicted by the simple Sverdrup relation and the mean wind stress curl field over the North Pacific (despite the complicated bathymetry and gaps along the North Pacific western boundary). Northeast of Luzon, the Kuroshio—bounded by the 0 m s^{-1} isotach—is shallower than 750 dbar, while east of Taiwan areas of positive flow reach to the seafloor (3000 m). Both arrays indicate a deep counterflow beneath the poleward-flowing Kuroshio (−10.3 ± 2.3 Sv by Luzon and −12.5 ± 1.2 Sv east of Taiwan). Time-varying transports and velocities indicate the strong influence at both sections of westward propagating eddies from the ocean interior. Topography associated with the ridges east of Taiwan also influences the mean and time-varying velocity structure there.

1. Introduction

Similar to the Gulf Stream in the North Atlantic, the Kuroshio (Figure 1a) transports warm salty waters poleward in the western subtropical North Pacific [*Nitani*, 1972]. As part of the large-scale wind-driven circulation [*Sverdrup*, 1947; *Stommel*, 1948], the swift Gulf Stream and Kuroshio each contribute to the system of narrow western boundary currents that serve as the return flow for each basin's interior transport. This interior transport can be approximated with a linear, steady vorticity balance giving the "Sverdrup relation" for a homogenous, constant depth basin. The resulting interior Sverdrup transport, T_{Sv}. is the meridional flow in response to the wind stress curl integrated zonally from the eastern boundary:

$$T_{Sv}(x_w, y) = \frac{1}{\rho\beta}\int_{x_E}^{x_W} (\nabla_H \times \vec{\tau})dx \quad (1)$$

Here x and y are the zonal and meridional directions, ρ is the ocean's density, β is the meridional gradient of f, the Coriolis parameter (i.e., df/dy), $\vec{\tau}$ is the wind stress, and x_E and x_w are the eastern and western limits of integration. The corresponding steady solution for a layered ocean has the lower layer(s) at rest and the Sverdrup transport (and western boundary current return flow) confined to the upper layer [*Veronis and Stommel*, 1956; *Anderson and Gill*, 1975]. During the layered ocean's slow baroclinic adjustment to this steady state, the vertical distribution of Sverdrup transport in the layers can change, but for a uniform depth ocean, the net western boundary current return flow (vertically integrated over the layers) remains constant and in balance with the wind stress curl according to equation (1) even as the vertical structure of the western boundary current changes during the spin-up [e.g., *Andres et al*., 2012]. The adjustment period for a layered ocean with variable depth is more complicated (and the net western boundary current transport in the return flow can change with time even as the wind field remains steady during spin-up) because the effect

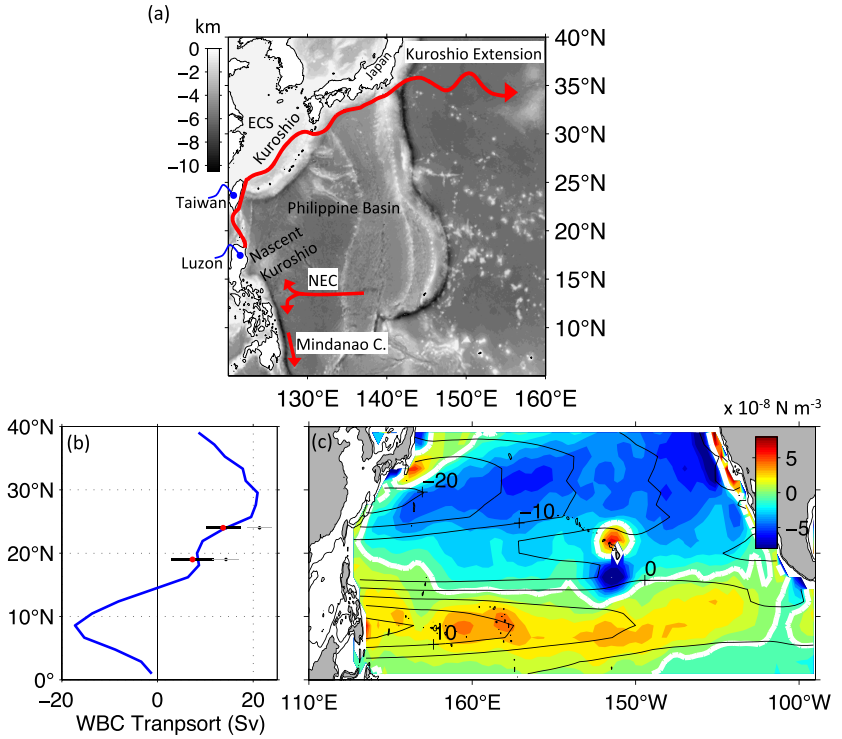

Figure 1. (a) Schematic of western boundary currents in the tropical and subtropical North Pacific superimposed on the bathymetry (km, shading). Kuroshio path is based on the mean absolute dynamic topography from satellite altimetry. ECS denotes the East China Sea and NEC the North Equatorial Current. (b) Theoretical western boundary current transport (blue curve) calculated as the return flow to the interior Sverdrup flow according to equation (1); red dots indicate the measured time-mean net transports (absolute geostrophic flows integrated from the surface to the bottom) observed by the moored arrays east of Taiwan (∼24°N) and northeast of Luzon (∼19°N) with each mean's standard error (mse) shown by the black lines; gray dots and lines indicate the means and standard errors of the absolute geostrophic transports in only the upper 1000 dbar at each array. (c) North Pacific mean wind stress curl (N m^{-3}, shading) calculated from the 1948–2012 monthly mean wind stress from the National Centers for Environmental Prediction-National Center for Atmospheric Research (NCEP-NCAR) reanalysis, which is available at ∼2° horizontal resolution [*Kalnay et al.*, 1996]. The mean wind stress curl zero contour is highlighted in white. The interior Sverdrup transport calculated from equation (1) is superimposed (black contours). Contour intervals are at 5 Sv increment (1 Sv = 10^6 m^3 s^{-1}) with positive (negative) values indicating northward (southward) interior flow.

of the wind stress curl is determined by integrating along potential vorticity characteristics f/h_L (where h_L is a layer thickness) rather than integrating zonally [e.g., *Andres et al.*, 2011].

Observed features of the North Pacific subtropical gyre (Figure 1a) are broadly consistent with the North Pacific mean wind stress curl pattern (Figure 1c, shading) and the Sverdrup relation (black contours). The Kuroshio forms near Lamon Bay, Philippines [*Gordon et al.*, 2014], from the northern branch of the westward-flowing North Equatorial Current, which bifurcates around 14°N [*Qiu and Chen*, 2010]. Downstream of its origin, the Kuroshio travels along the western boundary [*Andres et al.*, 2015] toward southeastern Japan where the current finally separates from the boundary to become a free jet, the Kuroshio Extension. Equation (1) and the North Pacific mean wind stress curl pattern predict a poleward western boundary current return flow that intensifies from about 8.5 Sv east of Luzon at 19°N to 14 Sv east of Taiwan at 24°N (Figure 1b, blue curve). While, previous observational studies do confirm a downstream intensification of the Kuroshio here, the magnitudes of the reported time-mean transports are somewhat larger than those predicted by equation (1), possibly because the observations sampled only the upper ocean and/or because the western boundary is complicated with ridges and gaps. East of Luzon, the observed Kuroshio mean transport is 15 Sv (with standard deviation, σ, of $\pm$3 Sv). This reported transport is integrated over just the regions of poleward flow in the upper 600 dbar and was measured by six upward-looking ADCPs from June 2012 through June 2013 (*Lien et al.* [2014] with the velocities below the 450 m mooring depth extrapolated). Downstream, the 20 month mean Kuroshio transport (September 1994 through May 1996) derived from the WOCE PCM-1 moored current meter array across the Ilan Ridge is 21.5 $\pm$ 2.5 Sv [*Johns et al.*, 2001]. The mean velocity structure at the Ilan Ridge where the Kuroshio

funnels into the East China Sea (sill depth = 775 m) suggests positive (poleward) flow over the entire Ilan Ridge [from *Johns et al*., 2001, Figure 5].

Individual synoptic sections across the Kuroshio from shipboard measurements and from moorings exhibit significant temporal variability in transport and velocity structure [e.g., *Jan et al*., 2015; *Lien et al*., 2014; *Andres et al*., 2008b] and associated nutrient transport [*Chen et al*., 2017]. Whether (and how) variability in Kuroshio transport and velocity structure at one latitude is related to Kuroshio variability at other latitudes may depend on the time scale considered. Kuroshio transport varies with about 100 day period northeast of Taiwan [*Johns et al*., 2001; *Zhang et al*., 2001] and with slightly shorter period northeast of Luzon [*Lien et al*., 2014] due to frequent arrivals of westward propagating features from the ocean interior at both locations. These propagating features—collectively called "eddies" here—are readily apparent as sea surface highs and lows in successive maps from satellite altimetry [e.g., *Chelton et al*., 2007] with about six arrivals per year by Taiwan and about eight per year by Luzon [*Tsai et al*., 2015; *Lien et al*., 2014]. At these eddy time scales, variability in the Kuroshio at one latitude does not seem to be communicated downstream very effectively by the current. Indeed, in a study period that comprised five eddy arrivals east of Luzon, *Tsai et al*. [2015] find evidence of only one anticyclonic eddy that first affected the sea surface height and pycnocline depth on the Kuroshio's offshore edge in the region northeast of Luzon and then 21 days later 500 km downstream east of Taiwan. Other eddy events seem to change the strength of the local recirculation but do not have a clear effect on the Kuroshio throughput to other latitudes.

At interannual periods, Kuroshio variability may be communicated more effectively across latitudes as signals propagate equatorward (opposite the Kuroshio flow) along the western boundary. For example, interannual variability of the large-scale wind field in the interior North Pacific around 37°N is well correlated with sea surface height along the onshore side of the Kuroshio throughout the East China Sea [*Andres et al*., 2011]. In this case, barotropic variability is not advected by the Kuroshio (as a salinity anomaly or a drifter might be) but propagates first from the wind-forced region to the western boundary along an f/h contour (where h is the total water depth) and then propagates equatorward in the waveguide to conserve potential vorticity [*Andres et al*., 2011] as h decreases onshore. Results from a data-assimilating model suggest that such low frequency variability can be masked in years with enhanced mesoscale eddy activity [*Soeyanto et al*., 2014].

In contrast to this example of wind-forced variability that propagates equatorward in the waveguide, low frequency variability may also be advected downstream (poleward) within the Kuroshio. East of Luzon, the bifurcation latitude of the North Equatorial Current (which feeds the northward-flowing Kuroshio and the southward-flowing Mindanao Current) migrates at interannual to decadal scales between 10°N and 15°N [*Qiu and Chen*, 2010]. Repeated glider sections across the Kuroshio near 19°N suggest that Kuroshio strength northeast of Luzon is significantly negatively correlated with the bifurcation latitude: as the bifurcation point moves northward, the Kuroshio transport decreases [*Lee*, 2015]. However, evidence for a similar negative correlation between bifurcation latitude and Kuroshio strength further downstream (e.g., east of Taiwan near 23°N) is equivocal, due in part to the strong variability at eddy time scales east of Taiwan [*Lee*, 2015].

Here we examine the mean and time-varying Kuroshio strength and velocity structure and the current's spatial evolution between Luzon, Philippines, and eastern Taiwan as measured by pressure-sensor equipped inverted echo sounders (PIESs). The observations discussed here are part of a data set—remarkable in its duration, spatial coverage, and the combination of measurement platforms—collected through international collaborations under the Origins of the Kuroshio and Mindanao Current (OKMC) program and the Observations of Kuroshio Transport Variability (OKTV) program funded respectively by the U.S. Office of Naval Research and the Ministry of Science and Technology (MOST), Taiwan, R.O.C. While elements of this OKMC/OKTV data set have been published previously (see the specific references throughout the text and also the *Oceanography* special issue: "A New Look at the Low-Latitude Western North Pacific") [*Rudnick et al*., 2015], this work represents the first report of the time series of the full-water column absolute transports and velocities east of Taiwan generated from the PIESs' observations and the first analysis comparing these results with the analogous time series derived from PIESs deployed across the Kuroshio northeast of Luzon. In addition to the PIES bottom landers, the OKMC/OKTV data used here comprise in situ observations from tall moorings, autonomous platforms, and shipboard measurements. The data sets are introduced in section 2 (with the records from the PIESs included in Appendix A). Section 3 briefly describes the methodology

used to process the PIES data to obtain the time-varying velocities and transports (with further details given in Appendices B and C). Section 4 presents the results for the Taiwan array and examines the downstream evolution of the Kuroshio by comparing these results with those from the Luzon array. Section 5 discusses the role of eddies and topography in shaping the mean and time-varying flow structure east of Taiwan. Section 6 summarizes the main findings of this study.

2. Data

2.1. The Taiwan and Luzon Arrays

Instruments were deployed across the Kuroshio northeast of Luzon, Philippines, for 12 months (9 June 2012 to 1 June 2013) and east of Taiwan for 23 months (14 November 2012 to 31 October 2014), giving an 8 month overlap in measurements from the two arrays (November 2012 to June 2013). Both arrays included PIES bottom landers and moorings with upward-looking acoustic Doppler current profilers (ADCPs). Water depths and locations for the instrument sites are summarized in Table 1.

The array east of Taiwan comprised three tall moorings—each with an upward-looking ADCP at 500 m depth—and six PIES bottom landers (Figures 2a and 2b). The ADCPs and four of the PIESs were deployed across the Kuroshio at ~23.75°N spanning 135 km along the Yaeyama Ridge. This ridge is 50 km upstream of the Ilan Ridge. The latter marks the Kuroshio's entrance into the East China Sea between northeastern Taiwan and Ishigaki Island. The remaining two PIESs of the Taiwan array were deployed in a meridional section along 123°E on the offshore side of the Kuroshio extending 100 km southward from the main line of instruments into the Philippine Basin. Water depths at the instrument sites east of Taiwan (identified with the prefix "T-") range from 2300 m depth at the onshore-most ADCP mooring site (T-A1) to almost 6000 m depth at one of the PIES sites in the Philippine Basin interior (T-P5).

Table 1. Instrument Locations and Depths

Site ID	Type	Lat (°N)	Lon (°E)	Water Depth (m)[a,b]	Distance (km)[c,d]	Spacing (km)
Array East of Taiwan[e]						
T-A1	ADCP	23.875	121.720	2282.0		
T-A2	ADCP	23.813	122.000	2553.0	29.3	29.3
T-A3	ADCP	23.743	122.352	2917.0	65.9	36.6
T-P1	PIES	23.843	121.854	4171.8	14.1	
T-P2	PIES	23.779	122.185	2531.1	48.5	34.4
T-P3	PIES	23.695	122.610	2656.7	92.7	44.2
T-P4	CPIES	23.616	122.997	2253.0	133.0	40.3
T-P5	PIES	23.136	123.003	6031.7		53.3
T-P6	PIES	22.757	123.000	4512.4		42.1
Array Northeast of Luzon[f]						
L-M1	ADCP	18.750	122.100	980.0		
L-M2	ADCP	18.750	122.250	1035.0	15.8	15.8
L-M3	ADCP	18.750	122.400	1100.0	31.6	15.8
L-M4	ADCP	18.750	122.550	1675.0	47.3	15.8
L-M5	ADCP	18.750	122.680	2530.0	61.0	13.7
L-M6	ADCP	18.750	122.870	4465.0	81.0	20.0
L-H1	HPIES	18.812	122.011	1378.2		
L-H2	HPIES	18.826	122.308	1337.8	31.6	31.6
L-H3	HPIES	18.792	122.645	2076.8	66.3	35.0
L-H4	HPIES	18.852	122.952	4570.2	99.0	33.3
L-H5	HPIES	19.100	122.417	2151.8		

[a]ADCP depths are from Taiwan Ocean Database bathymetry.
[b]For the PIESs, depths are from the mean of pressure record less 0.5 m (distance between the pressure sensor and base of the instrument) and less atmospheric pressure.
[c]Cross-line distance reported relative to T-A1 for the Taiwan-array ADCPs and PIESs.
[d]Cross-line distance reported relative to the L-M1 for the ADCPs and L-H1 for the PIESs.
[e]Data records span 14 November 2012 to 31 October 2014, except for T-P4 which spans 14 November 2012 to 13 June 2014, and T-P1 whose data were recovered through 2 July 2014.
[f]Data records span 11 June 2012 to 1 June 2013.

The array east of Luzon spanned 100 km along 19°N from 122°E to 123°E and comprised six tall moorings with upward-looking ADCPs at 450 m depth and four PIES bottom landers (Figures 2c and 2d). A fifth PIES was deployed 30 km downstream (north) of this zonal section slightly east of the mean position of the Kuroshio core. The instruments sites (identified with the prefix "L-") were in water depths ranging from 1000 m near Camiguin Island on the onshore side of the array to 4500 m on the offshore side of the array (Table 1). The PIES line and ADCP line were offset slightly in the meridional direction, with PIESs along 18.80°N and ADCPs along 18.75°N, though here the data are treated as if they were collected along a single line.

Acoustic travel time data collected by the 11 PIESs from the Taiwan and Luzon arrays have been examined previously to investigate the effect of mesoscale eddies on pycnocline displacements [*Tsai et al.*, 2015] but their effect on transports or velocity structure has not yet been reported. In the present study of Kuroshio connectivity and downstream evolution, the mean and time-varying velocity structure and transport determined from the Taiwan-array PIESs are reported for the first

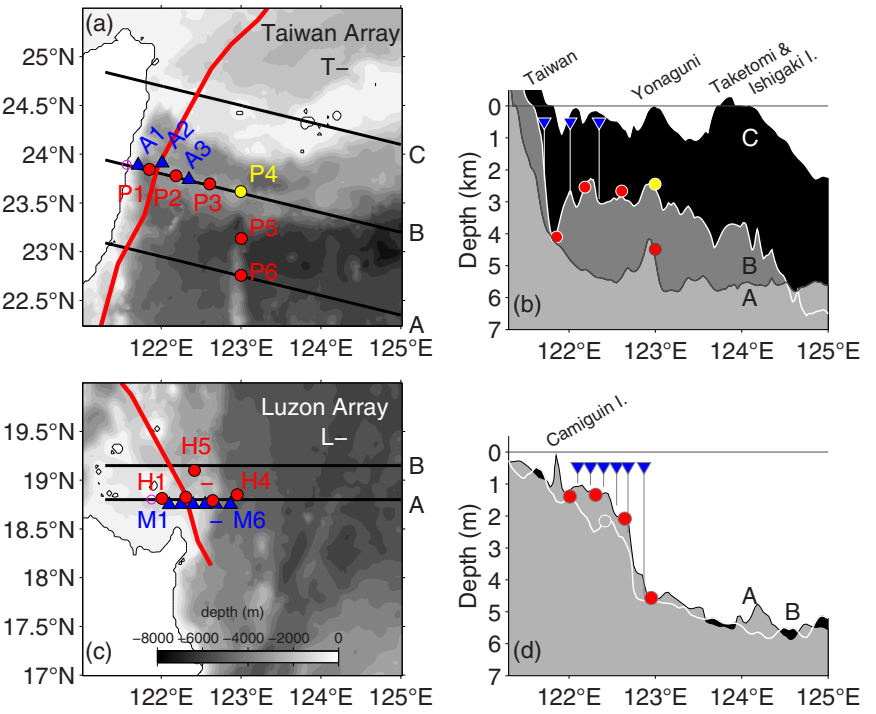

Figure 2. Maps and depth-longitude sections for the arrays (a, b) east of Taiwan and (c, d) northeast of Luzon. Symbols indicate upward-looking ADCPs (blue triangles), PIESs (red circles), and a CPIES (yellow circle). In Figures 2a and 2c, the red curves indicate a climatological mean Kuroshio path based on the velocity maximum observed from shipboard ADCP measurements [*Jan et al*., 2015] and the shading shows the bathymetry (m). In Figures 2a and 2b, the B-line is across the Yaeyama Ridge and the C-line is along the Ilan Ridge.

time and are compared to analogous results reported previously for the Luzon array [*Mensah et al*., 2016; *Lien et al*., 2014].

2.2. PIESs

A PIES rests on the seafloor in a rigid anchor stand and records the time-varying, round-trip surface-to-bottom acoustic travel time τ, near-bottom pressure P_b, and temperature T_b. The PIESs in the Taiwan and Luzon arrays were programmed to obtain hourly measures of τ, P_b, and T_b. One of the Taiwan PIESs (at site T-P4) was further equipped with an Aanderaa 4930 acoustic Doppler head to measure hourly horizontal currents (u, v) 50 m above the bottom (called a "CPIES"). The five PIESs northeast of Luzon were each equipped with a horizontal electric field (HEF) sensor (e.g., "HPIES,") [*Lien et al*., 2015]. The HEF provides a measure of the vertically integrated velocity at each HPIES site [*Sanford*, 1971; *Szuts*, 2012], though these HEF data are not included in the analysis here.

Data returns from the 11 Luzon and Taiwan PIESs (see Appendix A) are generally excellent except for a noisy travel time record at site L-H3, though the pressure record from this site is complete and of good quality. Also, the CPIES at site T-P4 ceased measuring 140 days before the end of its 2 year deployment (due to a drained system battery) but was successfully retrieved on the recovery cruise since the release batteries operate on a separate circuit. At this site (T-P4), the τ, P_b, and T_b and velocity data covering the first ~1.5 years of the deployment are complete and of good quality. The instrument at site T-P1 was not recovered, likely because the instrument was shifted by small earthquakes in the region [*Tsai et al*., 2015]. However, data from all of the Taiwan PIESs were retrieved periodically via telemetry during cruises, so telemetered τ, P_b, and T_b records (which are daily averages) are available for T-P1 through July 2014. The pressure record from site T-P1 is of good quality throughout the telemetered record except during the first 2 months of the deployment. The travel time record is good for the first 12 months of the mission; thereafter, the travel time record is noisy during stretches, and it is suspected that shifting sands here may have degraded the travel time record during some intermittent periods. During periods with missing data, pressure and travel time values are estimated via objective mapping of the data from neighboring sites (see Appendix B).

For each array, the raw τ records measured by the instruments, τ_{meas}, are converted to reference values, τ_{ref} (Figure A1), by using deep hydrographic casts from the region to establish the deep ocean's contribution to τ_{meas} [*Andres et al*., 2005]. Since deep-ocean temperature and salinity (and hence sound speed) vary little, this relationship is primarily controlled by the (time-invariant) vertical distance between the instrument depth and the reference depth. The conversion to τ_{ref} at each site allows comparison and processing of data from instruments that are generally deployed at different isobaths across the array. This reference level is then also used to generate the lookup tables used to interpret the travel time data (see section 2.4). For the Luzon array, 800 dbar is used as a reference (as previously reported in *Mensah et al*. [2016]) and here 1000 dbar is used for the array east of Taiwan.

2.3. ADCPs

Upward-looking 75 kHz acoustic Doppler current profilers (ADCPs) were deployed concurrently with the respective PIES arrays at 500 m depth east of Taiwan and 450 m depth northeast of Luzon. East of Taiwan, the spacing between ADCP moorings was ~33 km and the ADCPs measured at 5 min intervals and in 8 m vertical bins between 40 m depth and 500 m depth [*Y. J. Yang et al*., 2015]. Northeast of Luzon, the spacing was about 16 km and the ADCPs measured velocities at 1.5 min intervals in 8 m vertical bins between 45 and 450 m depth [*Lien et al*., 2014].

Details of the ADCP processing and results from the ADCP moorings are reported elsewhere [*Lien et al*., 2014, 2015; *Y. J. Yang et al*., 2015]. In the present study, the ADCP data are used for two purposes. First, time-mean velocities obtained from one depth bin from each ADCP are used to level neighboring pairs of PIESs' pressure sensors so that absolute transports and velocity profiles can be determined from the PIESs using the method described by *Mensah et al*. [2016] and in section 3.1. Second, the time series of absolute transports between the surface and 600 m depth (for the Luzon array) and 500 m depth (for the Taiwan array) are derived independently via only the ADCPs' velocity profiles (by integrating vertically and extrapolating the velocities between the bottom-most ADCP bin and the lower layer of integration). These ADCP transports are compared here with the transport time series (across the same area) derived from the leveled PIESs (see section 3.2 and Appendix C).

2.4. Seagliders

Seagliders instrumented with Sea-Bird CTDs measured temperature and salinity at 8 s interval from the surface to 1000 dbar in patterns near both arrays [*K.-C. Yang et al*., 2015]. Two Seagliders traversed the array east of Luzon between November 2012 and May 2013 providing 16 quasi-zonal property sections across the Kuroshio [*Lien et al*., 2015; *Mensah et al*., 2016]. From these sections, 1590 individual dives provided temperature and salinity profiles, which are used here to help construct the Gravest Empirical Mode (GEM) lookup tables that are used to convert PIESs' τ_{ref} time series to vertical profiles of density or specific volume anomaly [*Meinen and Watts*, 2000; *Sun and Watts*, 2001; *Watts et al*., 2001]. East of Taiwan, the Seagliders completed 10 Kuroshio crossings and contributed data from 1139 dives to that region's GEM lookup tables.

For the Luzon array, Seaglider data were also used as validation of the PIES processing methods (as reported previously in *Mensah et al*. [2016]). Seaglider-derived temperature cross sections were compared with the concurrent PIES-derived temperature cross sections to evaluate how well the PIESs' τ measurements interpreted via the GEM lookup tables could reproduce the depth of the thermocline across the Kuroshio. The agreement was found to be excellent [*Mensah et al*., 2016]. In addition, the agreement between Seaglider-derived absolute transports and PIES-derived absolute transports (to 1000 dbar) northeast of Luzon was favorable (see *Mensah et al*. [2016] and Appendix C).

2.5. Shipboard Observations

Seven shipboard surveys were conducted along the Yaeyama Ridge during the PIES deployment east of Taiwan as part of the OKTV effort (which comprised nine sections in total). During these crossings, hydrography (temperature and salinity profiles) and velocities across the Kuroshio were measured at eight stations between 121.72°E and 123°E (the KTV1 line as described in *Jan et al*. [2015]). At each station, measurements were collected from the surface to near bottom with a CTD and a 300 kHz lowered ADCP (LADCP). The hydrographic data from these cruises (together with historical hydrography and Seaglider casts) are used here to construct the GEM lookup tables for the Taiwan array. The LADCP sections are also used as an

independent check on the methodology used here to derive the transports from the PIESs east of Taiwan (section 3.2).

Further, LADCP data from six additional cruises collected through a follow-on study to the OKTV program (the Study of the Kuroshio-II, SK-II, funded by Taiwan's MOST) that have not been reported previously are used here with the nine OKTV sections [*Jan et al*., 2015] to produce a 15-section mean velocity structure to compare with the PIES-derived mean velocities at depths greater than those sampled by the gliders (section 4.1). The periods of the six additional ship surveys were 8–9 November 2014, 4–5 March 2015, 10–11 June 2015, 6–7 September 2015, 6–7 November 2015, and 30 June to 1 July 2016.

3. Methodology

The procedure to derive time series of a western boundary current's full-water column velocity structure and absolute geostrophic transports from the PIESs' τ and P_b records is well established [e.g., *Donohue et al*., 2010] and has been used successfully in many strong currents [e.g., *Book et al*., 2002; *Andres et al*., 2008b; *Beal et al*., 2015]. Due to the dependence of sound speed on temperature and salinity, τ is often an excellent proxy for a region's vertical profiles of specific volume anomaly α(z) and density ρ(z). Thus, pairs of PIESs can be used with the thermal wind relationship to deduce the vertical shear in the horizontal velocities normal to each instrument pair, $\delta v/\delta z$ [e.g., *Meinen and Watts*, 2000]. Further, this geostrophic shear can be referenced by using the bottom pressure gradients between pairs of leveled instruments to obtain time series of the absolute geostrophic velocity profiles, $v(z)$ [e.g., *Donohue et al*., 2010]. These velocity profiles are then integrated vertically and horizontally to calculate the time-varying absolute geostrophic transports.

We employ this technique here and use the Taiwan-array PIES data to determine the full-water column velocity structure and transports in the Kuroshio region. We then compare the upper ocean part of the PIES-derived transports east of Taiwan to independent estimates of upper ocean transport to validate the methodology. In section 4, the Taiwan-array results are compared with results from the Luzon-array PIESs. (Details of the Luzon-array PIESs' processing steps are described elsewhere [*Mensah et al*., 2016] but are similar to the methodology described here for the Taiwan array; validation of the Luzon-array results is also discussed by *Mensah et al*. [2016] and is briefly reviewed in Appendix C.)

3.1. PIES Data Processing

For the Taiwan array, hourly pressure and acoustic travel time records from each PIES (P_b and τ_{meas}) are despiked, dedrifted, and detided according to the standard procedures [*Kennelly et al*., 2007]. Using the methods outlined in *Andres et al*. [2005] and *Kennelly et al*. [2007], the hourly acoustic travel time records from each PIES, τ_{meas}, are first converted to τ_{ref}, then 3 day low-pass filtered, and finally mapped (see Appendix B). The filtered, mapped τ_{ref} time series are then used with the region-specific empirical lookup tables (GEMs) to obtain time-varying profiles of specific volume anomaly, $\alpha(z)$—or alternatively, density or temperature profiles, $\rho(z)$ or T(z). For the Taiwan-array PIESs, two modifications to the traditional processing methods are employed to interpret the travel time and pressure data.

First, to obtain the profiles of density (or specific volume anomaly) from τ_{ref}, a region-specific empirical lookup table is typically used (i.e., the GEM). However, rather than using a single GEM interpret the Taiwan array's travel time observations, two GEM lookup tables are used for the array, a main GEM and a GEM for the onshore-most site. This is necessary due to the distribution of small amounts of South China Sea Tropical Water (SCSTW) that leaks through the Luzon Strait and the Babuyan Channel [*Mensah et al*., 2014], which can lead to ambiguity in interpreting PIESs' travel time measurements from a single GEM. The salinity maximum, typically located around 150 m depth, is in general an excellent tracer of the tropical water masses in the region (see *Mensah et al*. [2014] and the four salinity profiles shown in Figures 3b and 3c). The presence or absence of SCSTW in this tropical water salinity maximum layer can cause very different temperature, salinity, and density profiles to be associated with the same acoustic travel time (e.g., Figures 3b and 3c). The mean salinity distribution at 150 m depth relative to the PIES sites is shown in Figure 3a. From this, it is apparent that the SCSTW is confined geographically to the western extremes of both arrays (evident as the relatively fresher water mass at this depth when compared to the West Philippine Sea Tropical Water, WPSTW). The effect of two GEMs was tested extensively for the region east of Luzon [*Mensah et al*., 2016].

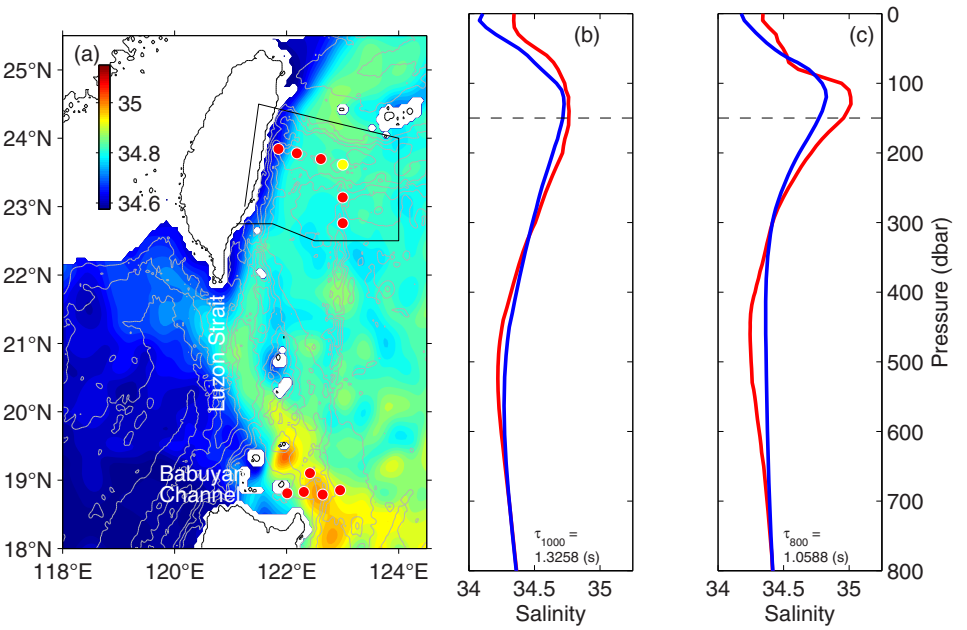

Figure 3. (a) Chart of mean salinity at 150 m depth (shading) around Taiwan and Luzon from a climatology based on data from the National Oceanographic Data Center (NODC), with much of these data from the Taiwan's Ocean Database (available at www.odb.ntu.edu). The regions of colder color west of the Kuroshio are strongly influenced by SCSTW [*Mensah et al.*, 2014]. PIES sites are also shown (red and yellow circles). (b) Examples of two salinity profiles from the region east of Taiwan with the same τ_{ref} (1.3258 s), but different vertical structure due to the presence of SCS waters in one (blue) and not in the other (red). (c) As in Figure 3b but for the region northeast of Luzon and for $\tau_{ref} = 1.0588$. The dashed lines in Figures 3b and 3c highlight the depth of the salinity distribution shown in Figure 3a.

Since improvement to the processing was found to be substantial, two GEM lookup tables are also used here in this study to interpret the data east of Taiwan. GEM information is summarized in Table 2.

The second modification to the traditional PIES processing is to use the upward-looking ADCPs for leveling the pressure records. (By leveling, PIES-measured bottom pressures are projected onto a common geopotential surface. Leveling is necessary for calculating horizontal gradients in the geostrophic equations.) Here the leveling depth is chosen as the depth where high quality time series of ADCP-measured velocities outside the upper Ekman layer are available (nominally between ~300 and 500 m depth). For the array northeast of Luzon, this method was used across the entire array (L-H1 through L-H4) and the leveling depth was 400 m (see *Mensah et al.* [2016] and Appendix C for validation of the method). For the array east of Taiwan, different leveling depths between different pairs of instruments provide the optimal results (300 m between T-P1 and T-P2, 500 m between T-P2 and T-P3). In addition, the bottom current meter is used to level between T-P3 and T-P4 (i.e., the traditional method is used here since there was no upward-looking ADCP between these two sites). The modified leveling method (i.e., leveraging the observations from the upward-looking ADCPs) for the Taiwan array gives Kuroshio transports, which compare favorably to independent LADCP-derived transports (section 3.2).

Table 2. GEM Information

	Lat. Limits (°N)	Lon. Limits (°E)	No. of Profiles
East of Taiwan			
Eastern Gem	24.25	122.75	1411
	24.00	124.00	
	22.70	124.00	
	22.70	122.50	
	22.75	121.75	
Western Gem	23.00	121.25	714
	24.50	121.50	
	24.25	122.75	
	22.75	121.75	
Northeast of Luzon			
Eastern Gem	18.67	122.30	1231
	19.25	122.30	
	19.25	123.50	
	18.67	123.50	
Western Gem	18.67	121.75	476
	19.25	121.75	
	19.25	122.30	
	18.67	122.30	

With these two modifications, we use the two GEMs and the mapped τ_{ref} to infer mapped density profiles east of Taiwan. From these, we calculate the baroclinic velocity sections along the Yaeyama Ridge. We use the mapped, leveled pressures (Appendix B) to reference this shear to obtain time series of absolute geostrophic velocity structure east of Taiwan at 10 km horizontal spacing and 1 dbar

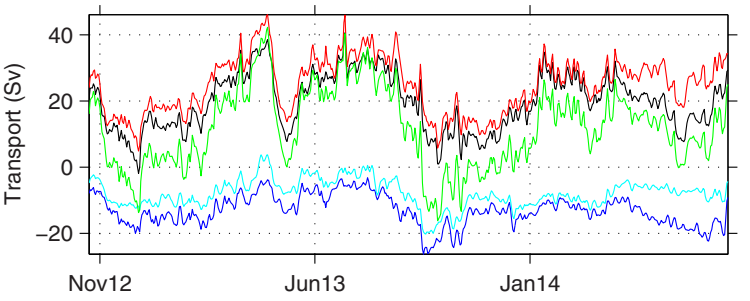

Figure 4. Results from the PIES array with transports east of Taiwan calculated by integrating velocities over various cross-sectional areas: positive transport (red), transport integrated from the surface to 1000 dbar (black), negative transport (blue), transport between 1000 dbar and the bottom (cyan), and the net surface-to-bottom transport (green), which is the sum of the positive and negative transports or, equivalently, the sum of the transports above and below 1000 dbar. Time series shown through July 2014; thereafter T-P4 stopped measuring.

vertical resolution from the surface to the bottom. We integrate these velocities vertically and horizontally to calculate transports across the Yaeyama Ridge east of Taiwan (Figure 4). An analogous procedure was carried out for the section northeast of Luzon by *Mensah et al.* [2016].

3.2. Comparison to Independent Estimates of Transport

As a test of the PIES processing methods east of Taiwan, transports deduced here from the PIESs are first compared to transports derived from the colocated ADCP moorings and then to transports determined from seven synoptic LADCP sections that were measured during the PIES deployment period [*Jan et al.*, 2015]. Similar comparisons between the Luzon-array PIES-derived transports and those from the ADCPs are detailed in *Mensah et al.* [2016] and are briefly described in Appendix C.

PIES-derived and ADCP-derived estimates of Kuroshio transport east of Taiwan are compared by integrating the respective velocity structures between 121.85°E and 122.43°E (spanning sites T-P1 to T-A3) but only in the upper ocean between the surface and 500 dbar (since the ADCPs could not measure the deep flow). Daily transports from the PIESs are compared with those from the upward-looking ADCPs over the full record, 14 November 2012 through 1 November 2014 (Figure 5, red and gray curves, respectively). The mean PIES-derived transport through the limited area defined above is 12.4 Sv ($\sigma = \pm 5.0$ Sv) and the mean upward-looking ADCP-derived transport through the same area is 12.3 Sv ($\sigma = \pm 3.7$ Sv). The root-mean-square (rms) difference between the transport estimates is 3.4 Sv (Table 3). The means are essentially the same and the rms difference may be due to the different measures of instantaneous Kuroshio strength and structure provided by the PIESs versus the moored ADCPs: each moored ADCP provides a point measure of the total (geostrophic plus ageostrophic) velocity structure while each pair of PIESs provides a spatial-average measure of the absolute geostrophic velocity structure between the instruments.

LADCP-derived transport snapshots from the OKTV program's seven synoptic sections measured during this period also compare favorably to the concurrent PIES-derived transports in the upper 500 dbar (Figure 5, magenta squares, with these transports also integrated over the upper 500 dbar, rather than over the full-depth of the LADCP profiles).

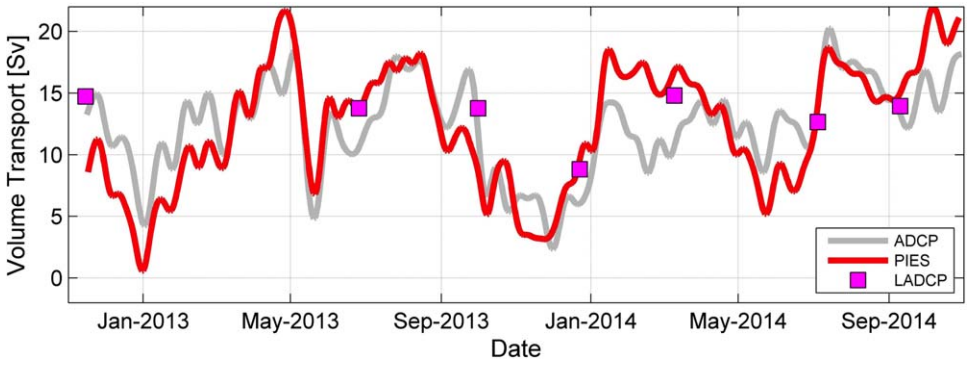

Figure 5. Comparison of upper ocean (<500 dbar) transports east of Taiwan calculated by different methods and platforms. The red curve is the PIES-derived absolute geostrophic transport and the gray curve is the ADCP-derived transport with transports 15 day low-pass filtered and spanning 121.85°E and 122.43°E. The magenta squares show the LADCP-derived transports [*Jan et al.*, 2015] integrated over the same area.

Table 3. Transport Comparisons

	Mean (Sv)	σ (Sv)	mse (Sv)	rms Difference (Sv)
East of Taiwan				
ADCP derived[a]	12.3	3.7		3.4
PIES derived[a]	12.4	5.0		
LADCP derived[b]	19.4	6.7	2.5	4.0
PIES derived[b]	21.4	6.0	2.3	
Northeast of Luzon[c]				
ADCP derived[d]	13.1	4.1		3.0
PIES derived[d]	14.2	4.9		
Seaglider derived[e]	12.1	3.9	1.0	1.8
PIES derived[e]	11.4	4.0	1.0	

[a]Integrated from the surface to 500 dbar between 121.85°E and 123.00°E.
[b]Integrated from the surface to 1000 dbar between 121.85°E and 123.00°E.
[c]From *Mensah et al*. [2016].
[d]Integrated from the surface to 600 dbar between 122.10°E and 122.87°E.
[e]Integrated from the surface to 1000 dbar between 122.10°E and 122.87°E.

Unlike the velocities from the upward-looking ADCPs (moored at 450 m depth), the LADCP sections also provide independent information about the deep-ocean velocity structure that can be used to assess the deeper PIES-derived velocities and transports. To compare PIES-derived transports and the LADCP survey transports, the domain considered is 121.85°E and 123.00°E (spanning T-P1 to T-P4) from the surface to 1000 dbar. Each LADCP section (spanning the same distance) comprises seven stations (K102 to K108) along the line east of Taiwan [*Jan et al*., 2015]. The PIES-derived mean of sections coincident spatially and temporally with the LADCP sections is 21.4 Sv (with a standard error, mse, of ±2.3 Sv, where each realization is treated as an independent measure of transport) and the LADCP-derived mean is 19.4 Sv (±2.5 Sv mse). The root-mean-square difference between the PIES-derived and LADCP-derived transports is 4.0 Sv (Table 3). As with the comparison made above between the (upward-looking) ADCP-derived transports and the PIES-derived transports to 500 dbar, the mean transports from these two independent estimates are very close (i.e., within the bounds provided by the means' standard errors). However, the PIESs measurements provide instantaneous snapshots across the array, while an LADCP survey typically takes several days to complete. This may alias the high frequency variability in the system and likely contributes to the rms difference between these transport estimates.

4. Results

With a good correspondence between the PIES-derived time-mean upper ocean transport estimates east of Taiwan (to 500 dbar and to 1000 dbar) and those from independent observations, we consider next the various components of the Kuroshio's full-water column mean and time-varying transports deduced from the PIESs (Figure 4) and compare these results with analogous observations of the Kuroshio upstream by Luzon to examine the downstream evolution of the Kuroshio. We show that the time-mean net transports integrated over the full-water column in the Kuroshio region are in good agreement with the return flow needed to balance the flows predicted by the simple Sverdrup relation integrated over the North Pacific interior (equation (1)). We also confirm that Kuroshio transport variability is dominated by the influence of mesoscale eddies.

4.1. Mean Transports

As mentioned in section 1, previous studies have shown Kuroshio intensification between 19°N and 24°N [*Lien et al*., 2014; *Johns et al*., 2001], but the magnitudes of these reported mean transports are too large to balance the interior Sverdrup flow for a flat ocean or for a fully adjusted ocean in which the lower layer(s) are quiescent. Our results from the PIESs corroborate a downstream increase in Kuroshio strength between the array northeast of Luzon and that east of Taiwan (Table 4). Northeast of Luzon, the Kuroshio's 12 month mean absolute transport integrated over the upper 1000 dbar is 14.3 Sv (±2.8 Sv mse). East of Taiwan along the Yaeyama Ridge, the Kuroshio's 23 month mean absolute transport integrated over the upper 1000 dbar is 21.3 Sv (±2.6 Sv mse), which is a 50% increase over that northeast of Luzon. The PIES-derived transports integrated over just the regions of positive (poleward) flow also increase downstream from 17.6 Sv (±2.5 Sv mse) northeast of Luzon to 26.2 Sv (±2.5 Sv mse) east of Taiwan. The increase in Kuroshio strength between Luzon and Taiwan inferred here from the PIES arrays is primarily associated with an increase in the thickness of the mean Kuroshio (depth to the 0 m s^{-1} isotach) rather than an increase in the speed of the current's mean velocity core. Northeast of Luzon, the mean Kuroshio's positive flow reaches to about 750 dbar with a negative (equatorward) counterflow below (Figure 6d). In contrast, east of Taiwan, there is an area of positive flow that reaches well below 1000 dbar and to the seafloor at 3000 m depth (Figure 6c).

Table 4. Mean Transports

	Mean (Sv)	Standard Deviation (Sv)	Decorrelation Scale (Days)	Mean Standard Error (Sv)	Range (Sv)
East of Taiwan (120 km Transect)					
Upper 1000 dbar transport	21.3	8.8	54	2.6	−1.9 to 40.7
Positive transport	26.2	8.6	60	2.5	4.9 to 46.1
Negative transport	−12.5	4.5	54	1.2	−26.3 to −3.2
Net transport	13.7	12.0	66	3.6	−16.2 to 42.3
Northeast of Luzon (100 km Transect)					
Upper 1000 dbar transport	14.3	6.8	54	2.8	−2.6 to 28.3
Positive transport	17.6	6.6	52	2.5	6.0 to 36.1
Negative transport	−10.3	7.7	32	2.3	−31.3 to 0
Net transport	7.3	13.3	37	4.4	−25.2 to 34.5

The observed downstream intensification of Kuroshio time-mean transports is not surprising and is expected from the Sverdrup relation and the mean wind field. However, as with the previous studies, the magnitudes reported here of the observed time-mean transports (whether in the upper 1000 dbar or

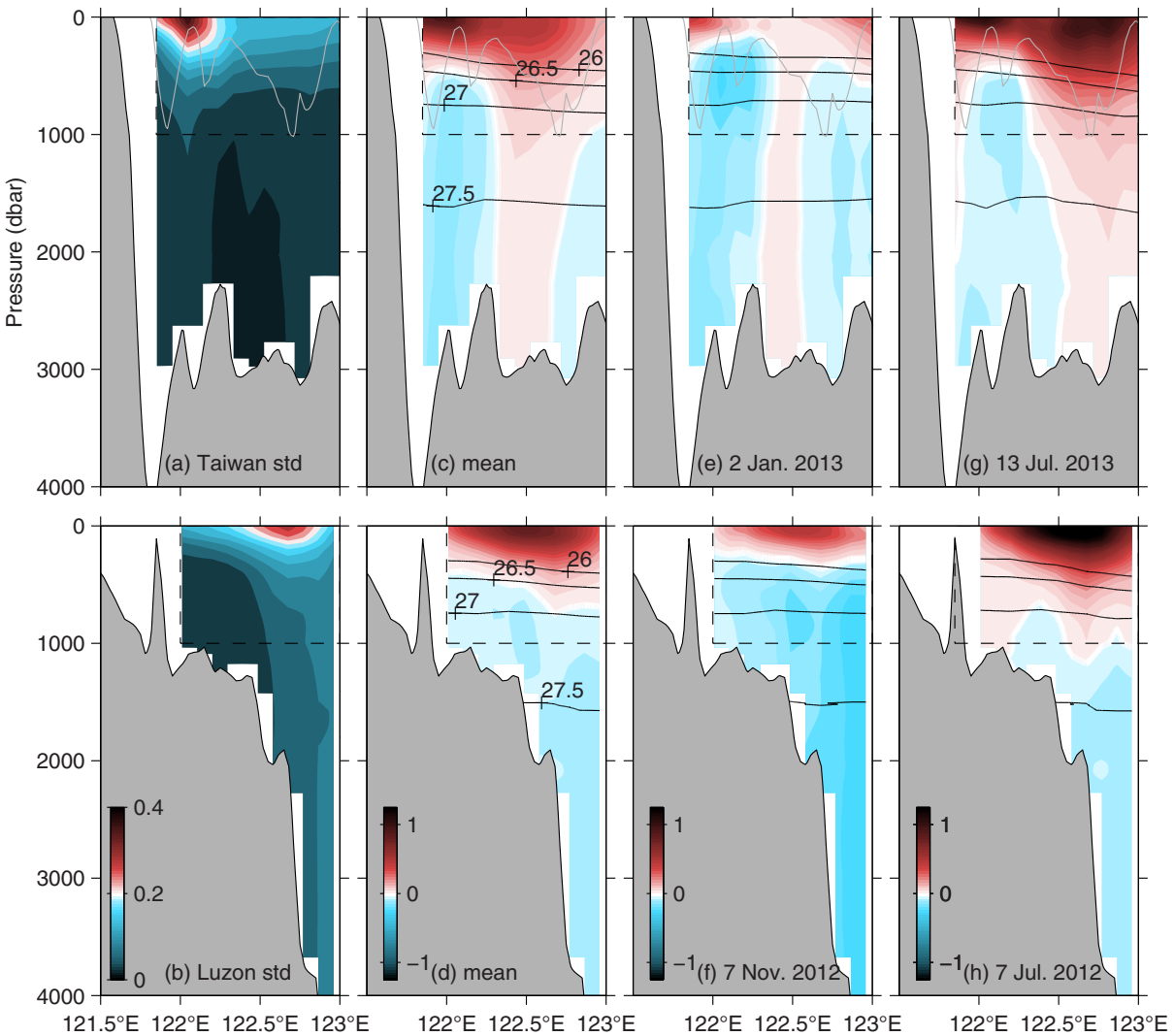

Figure 6. (a, b) Standard deviation (m s^{-1}) and (c, d) mean (m s^{-1}) of the velocity sections (top row) east of Taiwan and (bottom row) northeast of Luzon determined from the respective PIES arrays. Snapshot sections east of Taiwan are shown for the day with the (e) weakest and (g) strongest transport in the upper 1000 dbar (i.e., integrated within the dashed box) as are snapshot sections northeast of Luzon for the day with the (f) weakest and (h) strongest transport. In Figures 6c–6h, black contours show the respective potential density surfaces from 1026 to 1027.5 kg m^{-3} (referenced to 0 dbar). Gray line in the top row shows the bathymetry along the Ilan Ridge, which marks the entrance to the East China Sea.

integrated over all regions of positive flow) are large relative to those predicted from equation (1) (Figure 1b, compare black dots with the blue curve). In contrast, the PIES-derived *net* (surface-to-bottom) time-mean absolute transports reported here are remarkably consistent with the Sverdrup relation (Figure 1b, red dots). Northeast of Luzon the mean return flow predicted by equation (1) is 8.5 Sv and the PIES-observed surface-to-bottom mean absolute transport is 7.3 Sv ($\pm$4.4 Sv mse). East of Taiwan the predicted transport is 14 Sv and our PIES-observed mean is 13.7 Sv ($\pm$3.6 Sv mse). These results suggest that it is not the upper ocean western boundary current transport that is compensating the interior Sverdrup flow, but the total surface-to-bottom transport at the western boundary that serves as the return for the interior wind-driven transport. This result is consistent with *Anderson and Gill* [1975] who show that the wind-driven circulation is not confined to the upper layer (i.e., with lower layer(s) shut down) until the slow (westward propagating) baroclinic signals arrive from the wind-forced regions. The North Pacific is not in steady state but is continually undergoing baroclinic adjustment to the wind field. Apparently a correspondence between the magnitude of the predicted return flow (from a simple Sverdrup balance over the interior) and the observed western boundary current net transports holds despite the complicated bottom topography and the gaps along the western boundary (i.e., the Luzon Strait) where the Kuroshio encounters South China Sea waters on its cyclonic flank.

4.2. Mean Flow Structure

Complementing the Kuroshio's poleward flow through the East China Sea, the Ryukyu Current transports waters as a subsurface-intensified poleward flow along the southeastern side of the Ryukyu Islands. Ryukyu Current transport increases from about 6 Sv southeast of Okinawa [*Zhu et al*., 2003] to 18 Sv by Amami-Oshima [*Ichikawa et al*., 2004] where it joins the Kuroshio, which exits the East China Sea by the Tokara Strait. The Ryukyu Current structure near its origin southwest of Okinawa is not well studied.

After crossing the Yaeyama Ridge (where the Taiwan array is located), the deep part of the Kuroshio's poleward flow encounters the comparatively shallow Ilan Ridge (see the gray curve in the top row of Figure 6 and also the topographic sections in Figure 2b). The similarity of our mean Kuroshio transport in the upper 1000 dbar (21.3 Sv) crossing the Yaeyama Ridge to that reported previously crossing the Ilan Ridge (21 Sv) [*Johns et al*., 2001] suggests that little (if any) flow is diverted in the mean from the upper Kuroshio ($<$1000 dbar) to form the beginning of a Ryukyu Current. Though Kuroshio transport *above* 1000 dbar east of Taiwan does not seem to contribute to a mean Ryukyu Current, it is possible that some of the deep Kuroshio (i.e., the positive mean flow below 1000 dbar in Figure 6c) flows northeastward to feed a nascent Ryukyu Current, or that some flows as part of a deep anticyclonic recirculation east of the region sampled by our array. Additional observations would be required to confirm either scenario.

The PIES observations do suggest, however, that impingement of the deep Kuroshio on the Ilan Ridge may be the source of a counterflow (equatorward flow) across the Taiwan array that manifests itself in the mean velocity section as a subsurface velocity extreme between the region of deep poleward flow and the steep coast of Taiwan (Figure 6c). Velocities here reach $>$0.1 m s^{-1} equatorward flow in a patch stretching from 650 dbar to the seafloor centered on 122°E. Indeed, such a mean structure is corroborated by an independently derived mean (to 2000 dbar) from the 15 LADCP sections along the Yaeyama Ridge (Figure 7). Nine of these sections are from the OKTV program and six are from the SK-II program. The mean structure from these sections is similar to that from the PIESs (Figure 5c) with a deep-reaching Kuroshio and a deep negative (equatorward) flow shoreward of this. Though it is not conclusive from these data, this counterflow suggests a larger deep mean cyclonic recirculation, just upstream of the Kuroshio's entrance to the East China Sea.

In the time-mean section northeast of Luzon, deep negative (equatorward) flow is also present beneath the Kuroshio (Figure 6d). Although the magnitude is similar at the two sections (–12.5 $\pm$ 1.2 Sv east of Taiwan and -10.3 ± 2.3 Sv northeast of Luzon), the mean structure of the abyssal flow is different. As mentioned above, east of Taiwan the bulk of the deep, negative flow is sandwiched between Taiwan and the deep (poleward-flowing) Kuroshio. Northeast of Luzon, however, the region of negative flow is contiguous beneath the shallow Kuroshio and the strongest equatorward flow is on the offshore edge of the array.

4.3. Time-Varying Kuroshio Transports Near Luzon and Taiwan

The Kuroshio exhibits strong temporal variability in its velocity structure (Figures 6e–6h) and transport (Figures 8a and 8b). East of Taiwan, the transport integrated over just the region of positive (poleward) flow

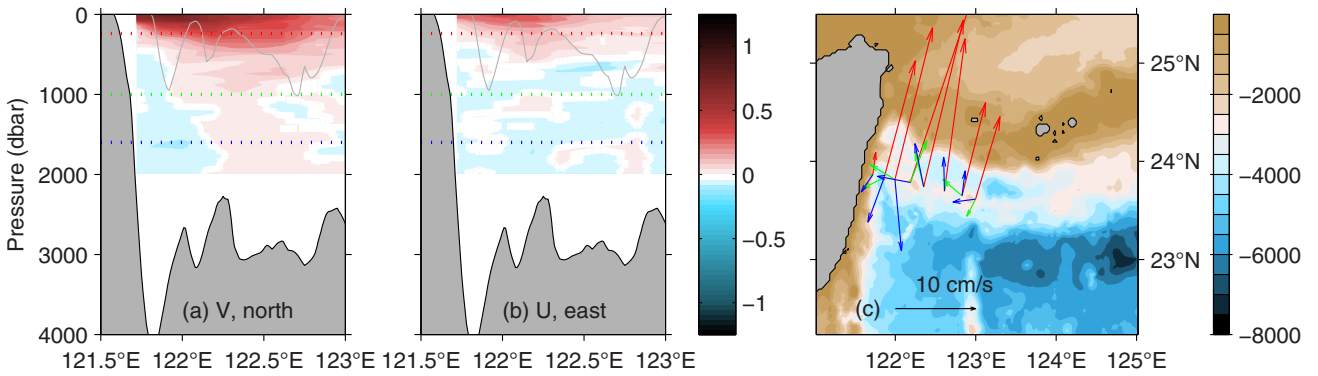

Figure 7. Mean (a) northward and (b) eastward velocity (m s^{-1}, shaded) generated from 15 LADCP sections along the Yaeyama Ridge. Gray curve denotes the sill of the Ilan Ridge (50 km downstream) and colored dashed lines indicate the depths of the velocity vectors shown in Figure 7c. (c) The bathymetry (m, shaded) with the mean velocity vectors at 240 m (red), 1000 m (green), and 1600 m (blue) depths superimposed.

varies from 4.9 to 46.1 Sv and the net transport integrated over the upper 1000 dbar here can be negative (e.g., −1.9 Sv on 2 January 2013, Figure 6e). This strong variability east of Taiwan is consistent with nine synoptic sections across the current east of Taiwan in which transport (integrated to the 0.2 m s^{-1} isotach) was found to range between 10.5 and 22.9 Sv [*Jan et al.*, 2015]. Variance preserving spectra for the upper ocean transport (to 1000 dbar) east of Taiwan (Figure 8c, blue) and northeast of Luzon (green) each have a broad peak around 30–100 days, with some of this energy likely due to the arrival along the boundary of westward propagating mesoscale eddies [*Tsai et al.*, 2015; *Lien et al.*, 2014; *Johns et al.*, 2001].

Northeast of Luzon, the variability in the positive and the upper ocean (to 1000 dbar) transports is slightly less pronounced than it is east of Taiwan (i.e., the standard deviations of these flows northeast of Luzon are smaller than their counterparts east of Taiwan, Table 4). In contrast, the negative transport (i.e., integrated over just the regions of negative flow) is more variable northeast of Luzon than it is east of Taiwan with a standard deviation almost twice as large ($\sigma = 7.8$ Sv northeast of Luzon and $\sigma = 4.5$ Sv east of Taiwan). This deep variability northeast of Luzon is particularly pronounced on the offshore side of the array (see the region of relatively high standard deviation at all depths in Figure 6b) and has an integral time scale of about 30 days. (In comparison, the other transport components here and east of Taiwan—positive flows, upper ocean flows, and negative flow east of Taiwan—each have an integral time scale of about 50–60 days.)

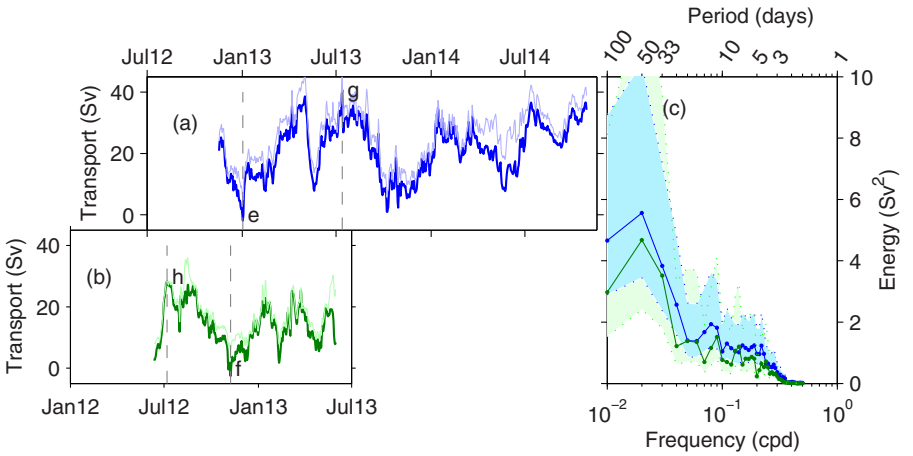

Figure 8. Variability in the Kuroshio upper ocean and positive transports observed with the PIES arrays. (a) Time series of transports east of Taiwan integrated from the surface to 1000 dbar (dark blue) and integrated over just the region of positive flow (light blue). (b) Time series of transports northeast of Luzon from the surface to 1000 dbar (dark green) and integrated over the region of positive flow (light green). In Figures 8a and 8b, the dashed lines show the timing of the velocity sections shown in Figures 6e–6h. (c) The variance preserving spectrum of the positive transport east of Taiwan (blue) and northeast of Luzon (green) with the respective 95% confidence limits shaded (the spectrum for the transport in the upper 1000 dbar, not shown, is similar).

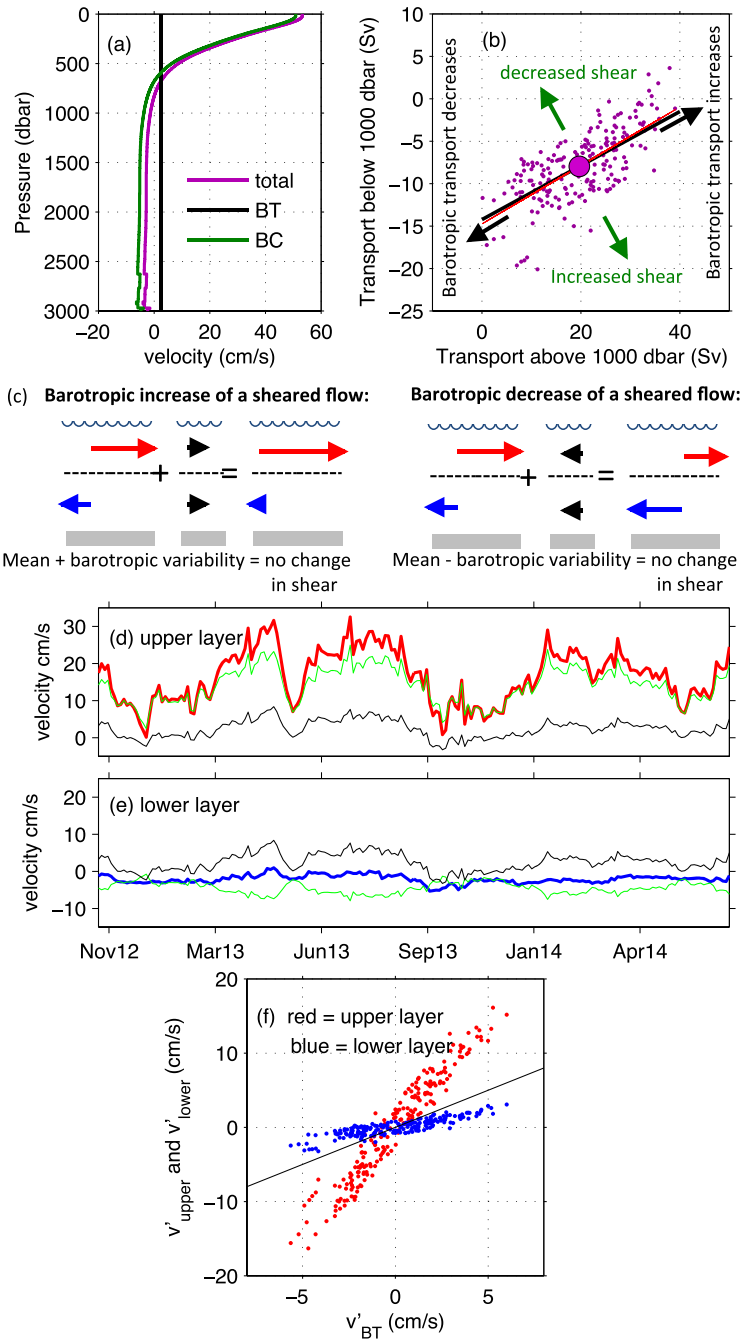

Figure 9. (a) Mean velocity profile east of Taiwan (purple) where the velocity at each depth is a horizontal average of the mean section shown in Figure 6b. The black line represents $<v_{BT}>$, which is $<T_{upper} + T_{lower}>/(A_{upper} + A_{lower}) = 2.4$ cm s^{-1} (similar to equation (6), but cast here for velocity rather than for velocity anomaly) and the green curve is the time-mean baroclinic shear profile relative to this mean barotropic reference velocity. (b) Upper and deep-ocean transports east of Taiwan (plotted for every third day, since the transports are derived from 3 day low-pass filtered data records) with the time-averages shown with the large purple dot. Black line is the best fit regression line (with $m = 0.34$) and the red line is A_{upper}/A_{lower} (with $m = 0.32$). Arrows indicate the effects on the layer transports of barotropic (black arrows) and baroclinic (green arrows) modes of variability. (c) Schematic of the barotropic variability implied by the correlation in Figure 9b superimposed on a sheared mean flow. (d) Time series of the velocity components in the upper layer east of Taiwan: v_{upper} (red), v_{BC} (black), and $v_{BC\ upper}$ (green). (e) Time series of the velocity components in the lower layer east of Taiwan: v_{lower} (blue), v_{BC} (black), and $v_{BC\ lower}$ (green). (f) Upper ocean (v_{upper}, red) and deep-ocean (v_{lower}, blue) velocity anomalies as a function of the barotropic velocity anomalies. Black line shows 1:1 ratio.

The strength of the variability of the western boundary current transport seems strongly related to the local geography. Downstream of both arrays at the PN line (northeast of Okinawa and within the East China Sea), the Kuroshio's reported standard deviation is only 4.0 Sv [*Andres et al.*, 2008b], which is less than that of the Kuroshio east of Taiwan or northeast of Luzon. Perhaps the standard deviations (Table 4) of the Kuroshio positive transports by Taiwan and Luzon ($\sigma = 8.6$ and 6.6 Sv, respectively) and of the transports in the upper 1000 dbar ($\sigma = 8.6$ and 6.8 Sv, respectively) are larger because the Kuroshio there is open to the direct influence of impinging westward propagating eddies. In contrast, within the East China Sea at the PN line, the Kuroshio is shielded from the open ocean eddies by the Ryukyu Island Chain. This suggests that much of the local variability in western boundary currents that is induced by impinging eddies leads to changes in local recirculation rather than changes in throughput that are subsequently felt downstream. While observations do suggest limited evidence of eddies that arrive at one latitude and then affect the transport at a downstream latitude, this downstream influence seems to be the exception rather than the rule [*Tsai et al.*, 2015].

5. Discussion

The mean Kuroshio east of Taiwan is surface intensified with strong vertical shear ($\delta v/\delta z$) to about 1000 dbar (Figures 6c and 9a, where the velocities in the latter are

horizontally averaged across the array to generate a single time-mean, spatial-mean velocity profile). The deep Kuroshio encounters the abrupt topography of the Yaeyama and the Ilan Ridges and the observations suggest strong coupling between the upper and deep ocean here. We examine the vertical structure of Kuroshio transport anomalies east of Taiwan and consider the effect of eddies and the role of topography in shaping the velocity structure along the western boundary.

5.1. Vertical Structure of Transport Anomalies East of Taiwan

To examine the temporal variability of transport anomalies superimposed on the time-mean vertical structure (Figure 9a, purple profile), we treat the Kuroshio as a two-layer system with the interface at 1000 dbar. The net (surface-to-bottom) transport is carried in the barotropic mode, so the time-average barotropic velocity east of Taiwan, $<v_{BT}>$, is the total mean transport across the array here divided by the cross-sectional area. This is 2.4 cm s^{-1}, represented by the black profile in Figure 9a (with the difference between the time-mean profile and this barotropic component giving a baroclinic component shown in green). Using a two-layer framework, the time-average layer shear, $<v_{upper} - v_{lower}>$, is 18.5 cm s^{-1} east of Taiwan.

East of Taiwan, the layer transports above and below the 1000 dbar interface (T_{upper} and T_{lower}) are positively correlated (Figure 9b, purple dots). The correlation coefficient, r, is 0.70 so almost 50% of the variance in T_{upper} is related to that in T_{lower} ($r^2 = 0.49$). T_{upper} is generally positive (i.e., poleward) and T_{lower} is negative. Thus, the positive correlation indicates that intensification in the upper layer is accompanied by a weakening of the lower layer transport. The opposite occurs when the upper layer transport becomes less intense and the negative transport in the lower becomes more intense. Though the Kuroshio's *mean* flow is strongly sheared, these correlations suggest a significant barotropic (vertically uniform) contribution to the Kuroshio's velocity variability (shown schematically for an idealized two-layer flow in Figure 9c). To assess this quantitatively, the total layer transports and total layer velocities are decomposed into barotropic and baroclinic components.

First, we consider the layer transports. The slope, m, of the linear regression between T_{upper} and T_{lower} (Figure 9b, black line) is 0.34. This slope is close to the ratio of the layers' cross-sectional areas: the area between the surface and 1000 dbar (A_{upper}) is 1.2×10^8 m^2 and the area between 1000 dbar and the seafloor (A_{lower}) is 3.8×10^8 m^2. Their ratio is 0.32. This area ratio A_{upper}/A_{lower} is represented by a line with $m = 0.32$ that passes through the time-mean layer transports (Figure 9b, red line passing through the purple filled circle). Since m of the best fit line is nearly equal to the area ratio of the layers, variability *along* the best fit line represents barotropic velocity anomalies that change the net transport (black arrows in Figure 9b). Variability *normal* to this line represents baroclinic velocity anomalies that change layer shear ($v_{upper} - v_{lower}$) but do not affect the net transport (green arrows in Figure 9b).

Next the layer-average velocity anomalies v'_{upper} and v'_{lower} are decomposed into baroclinic and barotropic components to examine their time-varying contributions to the current structure east of Taiwan. To decompose the observed transport variability east of Taiwan into a barotropic mode (i.e., associated with vertically uniform velocity anomalies, v'_{BT}) and a baroclinic mode (i.e., associated with vertically sheared velocity anomalies, $v'_{BC\ upper}$ and $v'_{BC\ lower}$), the time-varying, layer-average velocities are calculated from the PIES-observed transports:

$$v_{upper} = T_{upper}/A_{upper} \tag{2}$$

which is shown by the red curve in Figure 9d. In the lower layer:

$$v_{lower} = T_{lower}/A_{lower} \tag{3}$$

which is shown by the blue curve in Figure 9e. The layer-average velocity anomalies (v'_{upper} and v'_{lower}) each have baroclinic and barotropic components. For the upper layer:

$$v'_{upper} = v_{upper} - < v_{upper} > = v'_{BT} + v'_{BC\ upper} \tag{4}$$

where $< >$ is the time mean. The decomposition for the lower layer is analogous:

$$v'_{lower} = v_{lower} - < v_{lower} > = v'_{BT} + v'_{BC\ lower} \tag{5}$$

The net (integrated from the surface to the bottom) transport anomalies (i.e., $T'_{upper} + T'_{lower}$) are carried by the barotropic mode and the barotropic velocity anomalies are given by

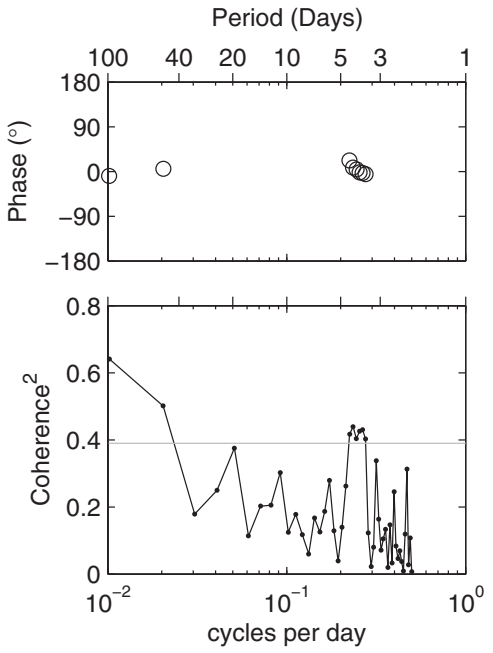

Figure 10. Spectrum of the squared coherence (bottom) between positive and negative transports at the PIES array east of Taiwan. The 95% confidence level is shown (gray line). The phases for the significant peaks (top) suggest zero lag between the time series at the coherent periods.

$$v\prime_{BT} = \left(T'_{upper} + T\prime_{lower}\right) / \left(A_{upper} + A_{lower}\right) \quad (6)$$

The time-varying v_{BT} east of Taiwan (which is equivalent in the two layers) is shown by the black lines in Figures 9d and 9e. Combining equations (4)–(6), one can then solve for the baroclinic velocities and baroclinic velocity anomalies in each layer (with $v_{BC\ upper}$ and $v_{BC\ lower}$ shown by the green lines in Figures 9d and 9e, respectively). Since a baroclinic transport anomaly in one layer is compensated by a baroclinic transport anomaly of equal magnitude and opposite sign in the other layer, the following relationship is set by the layers' area ratio:

$$v'_{BC\ lower} / v'_{BC\ upper} = -A_{upper} / A_{lower} = -0.32 \quad (7)$$

Finally, with the time-varying velocity anomalies in the layers (v'_{upper} and v'_{lower}) decomposed into v'_{BT}, $v'_{BC\ upper}$, and $v'_{BC\ lower}$, we consider how these covary. The results suggest strong coupling between the barotropic and baroclinic modes east of Taiwan. A substantial fraction of the variance of (total) velocities is associated with the barotropic mode. In both layers, v'_{BT} is strongly positively correlated with the total layer velocity (Figure 9f). In the upper layer, the (total) velocity anomalies are dominated by the baroclinic contribution, $v'_{BC\ upper}$ (indicated by the red dots in Figure 9f, which fall on a v'_{upper}:v'_{BT} line steeper than 1:1), but the total velocity anomalies are still strongly correlated with the barotropic variability (indicated by the tight distribution of the red dots and the high correlation of v'_{upper} and v'_{BT}, $r = 0.86$). In the lower layer, the velocity anomalies are dominated by the barotropic contribution (blue dots in Figure 9f). The correlation between v'_{lower} and v'_{BT} gives $r = 0.97$.

In the following section, we consider the arrival of eddies at the offshore (eastern) side of the Taiwan array. We argue that the tight coupling observed between upper ocean/deep-ocean variability (Figure 9b) and between barotropic/baroclinic modes of variability (Figures 9d–9f) is due to the structure of eddies.

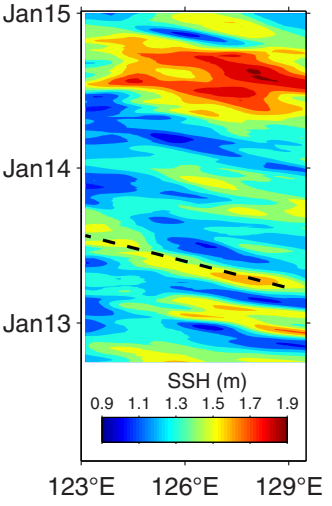

Figure 11. The time evolution of SSH (m, shaded) from altimetry along 23.375°N east of Taiwan. Dashed black line indicates signal propagation at 4.8 km d^{-1}.

5.2. Variability at Eddy Time Scales

The positive (poleward) and negative (equatorward) transports east of Taiwan (red and blue curves, respectively, in Figure 4) are coherent at eddy time scales (i.e., 50–100 day period, Figure 10, bottom) with zero lag between them at these periods (Figure 10, top, which shows only those cases where the coherence in the bottom figure is significant at the 95% level). This coherence at eddy time scales suggests that the barotropic variability depicted in Figure 9c is associated with eddy arrivals and that when eddies arrive east of Taiwan from the ocean interior they affect *both* the upper and lower layers. This in turn suggests that the sea surface height (SSH) anomaly associated with an eddy can comprise a barotropic and a baroclinic component (or a "mass loading" and a "steric" component) [*Baker-Yeboah et al.*, 2009]. This is consistent with a comparison of altimetry, acoustic travel time and bottom pressure, described below.

The arrival on the offshore edge of the Taiwan array at 123°E of eddies from the interior during the PIESs' deployment period is evident in a time-longitude plot of SSH from altimetry (Figure 11). The tilted phase lines here suggest a propagation speed of 4.8 km d^{-1} (indicated with the dashed line). The eddies' arrivals cause SSH at 123°E to vary by about ±30 cm (Figure 12a, black curve). As discussed by *Tsai et al.* [2015], the

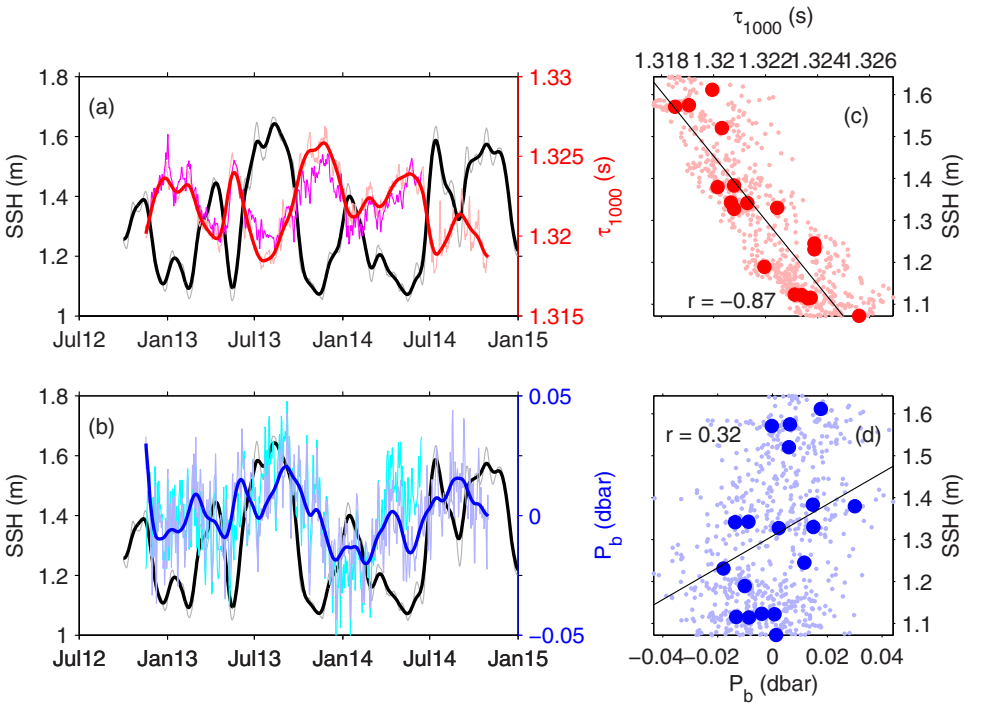

Figure 12. (a) Comparison of SSH and acoustic travel time records showing time series of the SSH (at 123°E, 23.375°N from the Aviso mapped absolute dynamic topography) daily product (gray) and with a 40 day low-pass filter applied (black). Also plotted is the time series of the 3 day low-pass filtered τ_{1000} from T-P5 (thin red) with a 40 day filter applied (red); the shorter τ_{1000} record from T-P4 is shown for comparison (magenta). (b) Comparison of SSH (as in Figure 12a) with the 3 day low-pass filtered P_b (with a time mean removed, but the basin mode retained, see Figure A2) from T-P5 (thin blue) and with a 40 day low-pass filter applied (heavy blue). The shorter P_b record from T-P4 is shown for comparison (cyan). (c) The negative correlation at T-P5 of SSH with τ_{1000} for the total signals (light red dots) and the 40 day low-pass filtered records (heavy red dots, plotted for every fortieth day). (d) The positive correlation at T-P5 of SSH with P_b for the total signals (light blue dots) and the 40 day low-pass filtered records (heavy blue dots, plotted for every fortieth day).

arrivals of SSH anomalies at the arrays east of Taiwan and northeast of Luzon are well correlated with anomalies in the PIESs' acoustic travel time records. This is because the eddies' SSH anomalies are generally accompanied by pycnocline displacements (which in turn affect the travel time observed with the PIESs due to the strong dependence of sound speed in seawater on temperature and salinity). East of Taiwan, SSH highs at the offshore side of the array at 123°E are accompanied by short travel times (and a depressed pycnocline) while SSH lows are accompanied by long travel times (and a shoaled pycnocline).

East of Taiwan, τ_{1000} and the local SSH (interpolated from the mapped satellite altimetry) are strongly anti-correlated at all of the offshore sites (T-P4 through T-P6). T-P5 is used for the analysis here even though T-P4 is on the main line of instruments along the Yaeyama Ridge because T-P5's records extend through the full 23 month deployment, allowing for a longer comparison to altimetry. (Note that T-P5's travel time and pressure records are very similar to those at T-P4, compare the thin light red and magenta curves in Figure 12a and the thin light blue and cyan lines in Figure 12b.) In addition to providing a longer record for comparison, T-P5 falls directly on a satellite altimeter track, which minimizes uncertainty in the SSH product related to the altimetry mapping errors.

At T-P5, τ_{1000} is strongly anticorrelated with SSH at eddy time scales (Figure 12a heavy black and red curves showing the 40 day low-pass filtered records). The correlation coefficient, r, between SSH and τ_{1000} is -0.87 for the unfiltered records (Figure 12c, light red dots) suggesting that 75% of the variance in SSH here is related to pycnocline displacements of opposite sign.

In contrast to the travel time, the bottom pressure anomalies at T-P5 are weakly *positively* correlated at eddy time scales with the SSH anomalies (Figure 12b heavy black and blue curves showing the 40 day low-pass filtered records). The correlation for the unfiltered records gives $r = 0.32$ (Figure 12d, light blue dots). This suggests that even though much of the variance in SSH is compensated by pycnocline displacements,

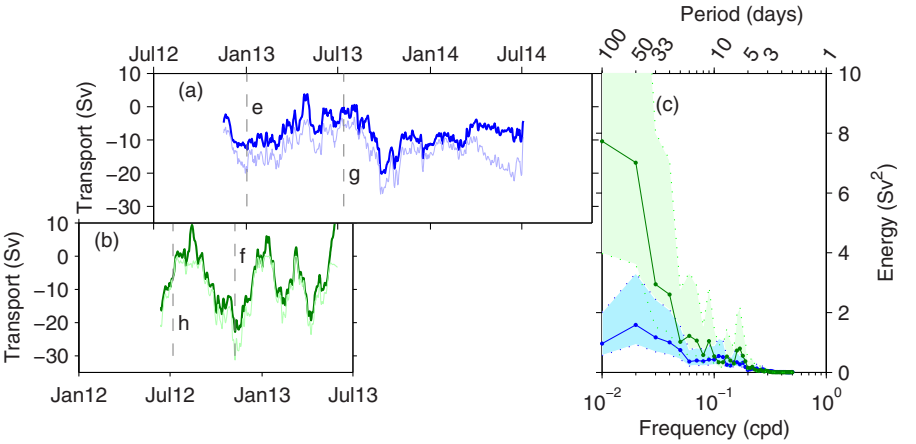

Figure 13. Variability in the Kuroshio counterflows. (a) Time series of transports east of Taiwan integrated from 1000 dbar to the bottom (dark blue) and integrated over the region of negative flow (light blue). (b) Time series of transports northeast of Luzon from 1000 dbar to the bottom (dark green) and integrated over the region of negative flow (light green). In Figures 13a and 13b, the dashed lines show the timing of the velocity sections shown in Figures 6e–6h. (c) The variance preserving spectrum of the transport below 1000 dbar east of Taiwan (blue) and northeast of Luzon (green) with the respective 95% confidence limits shaded.

about 10% of the variance in SSH is not compensated and causes bottom pressure anomalies (of the same sign as the SSH anomalies) when eddies arrive on the offshore edge of the Kuroshio.

These PIES observations confirm that these mesoscales eddies, though surface intensified and highly baroclinic, do have a deep structure and a barotropic component. Once the eddies reach the eastern edge of the array (and the eastern flank of the Kuroshio), their deep-reaching components begin to interact with the ridges east of Taiwan. Below we consider how this interaction shapes the flow.

5.3. The Role of the Ridges East of Taiwan

The deep-ocean pressure signals on the offshore edge of the array east of Taiwan discussed above are consistent with a modest peak observed at eddy periods in the variance preserving spectrum of deep transport (blue curve in Figure 13c). However, the variance preserving spectrum of the deep transport northeast of Luzon has an even more striking peak at eddy periods (Figure 13c, green curve). Below we argue that the topography east of Taiwan modifies the deep velocity structure when the onshore (western) edge of an eddy arrives at the offshore edge of the PIES array. We argue that the topography causes deep recirculation anomalies between the western edge of the eddy and Taiwan such that the compensating flows in the deep layer damp the peak in the transport spectrum at eddy time scales.

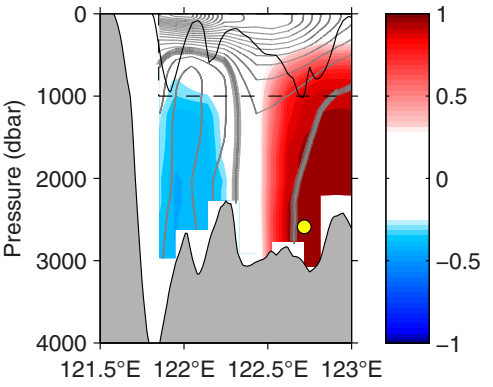

Figure 14. Cross section along the Yaeyama Ridge east of Taiwan showing the correlation coefficient (*r*, shaded) comparing the deep velocity at the eastern end of the array (yellow point) with the velocity at each other grid point. For reference, the gray lines show the mean velocity section (Figure 6c) with contour lines at 0.05 m s^{-1} interval and the zero contour shown with the heavy gray line. The thin black contour shows the sill of the Ilan Ridge, ~50 km downstream of the Yaeyama Ridge.

As discussed in section 4.2, the structure of the deep mean flow east of Taiwan (Figure 6c and reproduced in Figure 14 with the gray contours) suggests a deep cyclonic recirculation east of Taiwan arises because the mean deep positive (poleward) Kuroshio crosses the Yaeyama Ridge, impinges on the shallow Ilan Ridge, turns toward the Taiwan coast and then equatorward, crossing the Yaeyama Ridge as a negative flow between the deep Kuroshio and Taiwan. Indeed *variability* of the deep flow east of Taiwan is also consistent with this idea that recirculation is due to impingement of deep flows on the Ilan Ridge. Figure 14 is a correlation map with the color at each grid point showing the correlation between the local velocity and the deep velocity at the eastern end of the array (yellow dot). According to the correlation pattern (shading), when the deep poleward flow is strong near the eastern edge of the array (i.e., near

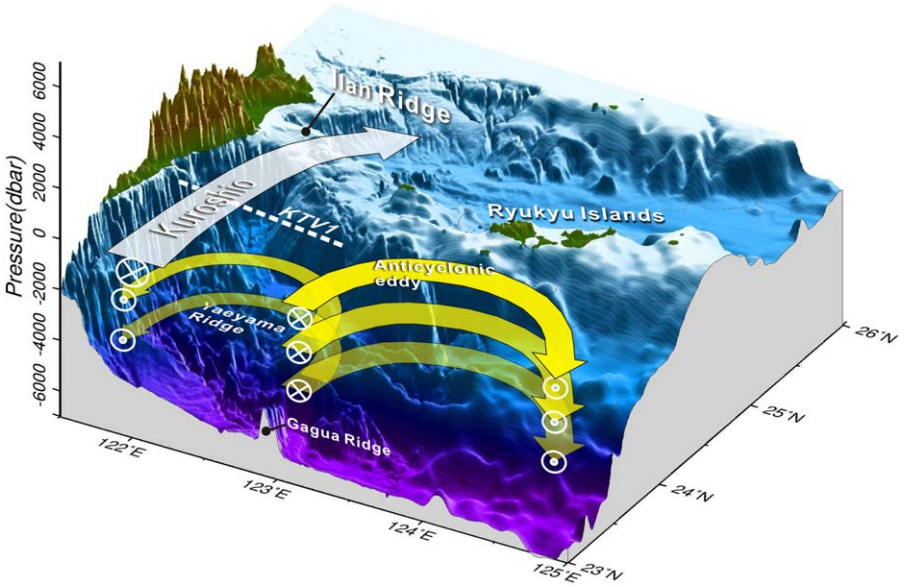

Figure 15. Schematic of a process that could lead to the correlation pattern in Figure 14. Here an anticyclonic eddy arrives on the offshore edge of the Kuroshio. The eddy, though surface intensified, does have a barotropic component to its flow. The deep part of the eddy's onshore edge impinges on the Ilan Ridge and some of the flow is diverted to turn counterclockwise so the flow returns across the Yaeyama Ridge (flowing equatorward between the Kuroshio's deep core and Taiwan). The offshore part of the eddy remains outside of the region sampled by the PIES array (the offshore-most PIESs are along 123°E).

122.5°E–123°E), flow at the western edge of the array (i.e., near 122°E) is strong and in the opposite direction (i.e., equatorward). One consequence of this is a compensation in the transport across the array below 1000 dbar: an increase in deep positive flow (presumably induced by the deep-reaching part of an anticyclonic eddy) is offset by an increase in deep negative flow so that the net transport below 1000 dbar is only weakly affected by the eddy. This mechanism is shown schematically in Figure 15 and is consistent with the relatively weak spectral peak at eddy periods (Figure 13e) for the deep flow east of Taiwan (blue) relative to that for deep flow northeast of Luzon (green) where there is no downstream ridge obstructing the deep flow.

6. Conclusions

The mean and time-varying velocity structure of the Kuroshio and its counterflows in the western Pacific between 18°N and 24°N are examined here by leveraging the measurement platforms used in the OKMC and OKTV field programs. This combination of measurements (from PIESs, upward-looking moored ADCPs, shipboard LADCPs and CTDs, and gliders) allows for validation of transport estimates, study of the flow's response to eddy arrivals from the ocean interior, and investigation of the effect of topography in shaping the mean flow structure east of Taiwan.

The Kuroshio's mean absolute transport in the upper 1000 dbar measured by the arrays increases downstream by 50% (from 14.3 $\pm$ 2.8 Sv northeast of Luzon to 21.3 $\pm$ 2.6 Sv east of Taiwan). This intensification occurs over roughly 500 km and is mainly attributed to a downstream increase in the mean depth of the isotachs as the Kuroshio entrains heavier South China Sea water from the west and lighter West Philippine Sea water from the east, leading to an increased pycnocline slope across the front [*Jan et al*., 2015]. In contrast to the transport in the upper 1000 dbar, the mean net (integrated from the surface to the bottom) transports are in good agreement with those predicted from the mean wind field and the (flat ocean) Sverdrup balance in the interior with the Kuroshio serving as the return flow to this interior, wind-driven flow. This simple result is surprising since the interior North Pacific is not flat and the lower layers are not at rest as the interior ocean is continually undergoing slow baroclinic adjustment to the wind field.

The mean Kuroshio transport east of Taiwan at the Yaeyama Ridge (2012–2014) and earlier estimates of the Kuroshio mean transport into the East China Sea (1993–1995) [*Johns et al*., 2001] suggest that most of the mean transport above 1000 dbar is effectively channeled over the Ilan Ridge and into the marginal sea.

There is likely a time-dependent eddy-driven steering of the flow between the Yaeyama and Ilan Ridges [e.g., *Yang et al*., 1999; *Zhang et al*., 2001; *Vélez-Belchí et al*., 2013] that diverts flow to contribute to a nascent Ryukyu Current along the Ryukyu Island Chain's southeastern side. This steering of the flow into the East China Sea Kuroshio or into a nascent Ryukyu Current is not resolved by the in situ observations discussed here but could be investigated further if a mooring array were deployed around 123°E–124°E between 23.5°N and the southwestern end of the Ryukyu Island Chain.

The structure of the mean and time-varying deep flows (>1000 dbar) inferred from the OKMC/OKTV observations highlight the importance of topography east of Taiwan where the effect of eddies on the deep transport is modulated by their interactions with the ridges that span the Kuroshio here (Figure 15). Eddies that arrive east of Taiwan have an expression in abyssal pressure anomalies (i.e., a barotropic or mass loading component in addition to their strong baroclinic or steric signature that is apparent in the acoustic travel times, Figure 12). As the shoreward (western) edge of an anticyclone arrives at the offshore side of the Kuroshio at the Yaeyama Ridge, deep flow impinges on the downstream topography (i.e., the Ilan Ridge), and a deep recirculation is induced on the *inshore* side of the array (with the counterflow here evident by the anticorrelated pattern of the deep flows Figure 14). The integrated effect of these positive and negative flows is to damp variability observed in the deep transport east of Taiwan. Northeast of Luzon, there is no analogous downstream blocking of the deep flow, so the eddies arrive and interact with the Kuroshio but their evolution is not shaped by flow impinging on a downstream ridge.

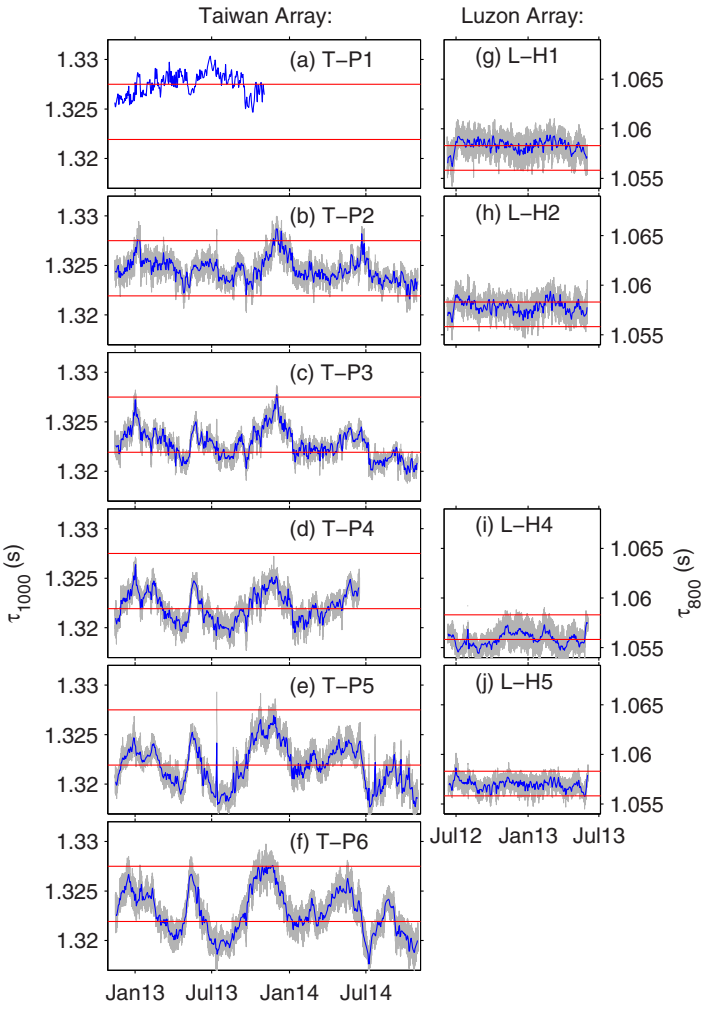

Figure A1. Hourly (gray) and 3 day low-pass filtered (blue) τ_{ref} records for the PIESs (a–f) east of Taiwan and (g–j) northeast of Luzon. In Figures A1a–A1f, the red lines show the Taiwan array's maximum and minimum record-mean τ_{1000} (which are obtained at T-P1 and T-P5, respectively). In Figures A1g–A1j, the red lines show the Luzon array's maximum and minimum record-mean τ_{800} (obtained from L-H1 and L-H4, respectively). Though the absolute τ_{ref} values vary across the two arrays because of the different reference levels used (1000 dbar east of Taiwan and 800 dbar northeast of Luzon), the ranges plotted in all figures are equal (0.015 s) so the amplitudes of variability can be easily compared within each array and between the Luzon and Taiwan arrays.

Appendix A: Comparison of Taiwan-Array and Luzon-Array PIES Data

The acoustic travel times (converted to τ_{ref}, see section 2.2) and pressure records from the Taiwan and Luzon-array PIESs are compared in Figures A1 and A2. The range ($\Delta\tau$) in site-averaged τ_{ref} values observed across the array east of Taiwan is larger than that observed northeast of Luzon: $\Delta\tau$ is 5.6 ms between T-P1 and T-P5 and 2.5 ms between L-H1 and L-H4 (Figure A1, red lines). This suggests a more steeply sloped pycnocline (and thermocline) across the Kuroshio east of Taiwan than northeast of Luzon and is consistent with a stronger Kuroshio east of Taiwan than northeast of Luzon. This downstream

intensification occurs as the Kuroshio entrains heavier South China Sea water from the west (associated with longer travel times) and lighter West Philippine Sea water from the east (associated with shorter travel times, leading to an increased pycnocline slope (larger $\Delta\tau$) across the Kuroshio [*Jan et al*., 2015]. In addition, the variability within each site's τ_{ref} time series is larger for the sites east of Taiwan (a–f) than for the sites northeast of Taiwan (g–j). This higher variance translates to a higher upper ocean transport variance observed east of Taiwan than northeast of Luzon.

In contrast to the travel time records, which have larger range and variance east of Taiwan than northeast of Luzon, the pressure records' ranges and temporal characteristics are more consistent across the arrays (Figure A2). However, each region does have a unique basin mode (i.e., a pressure signal that is common across the array's sites, Figures A1g and A1l). This is removed for the processing, because it is the time-mean and time-varying pressure *gradients* (rather than the absolute pressures) that are needed to calculate geostrophic velocity and transport but is included in the comparison of bottom pressure signals and SSH from satellite altimetry (section 5.2, Figure 12b).

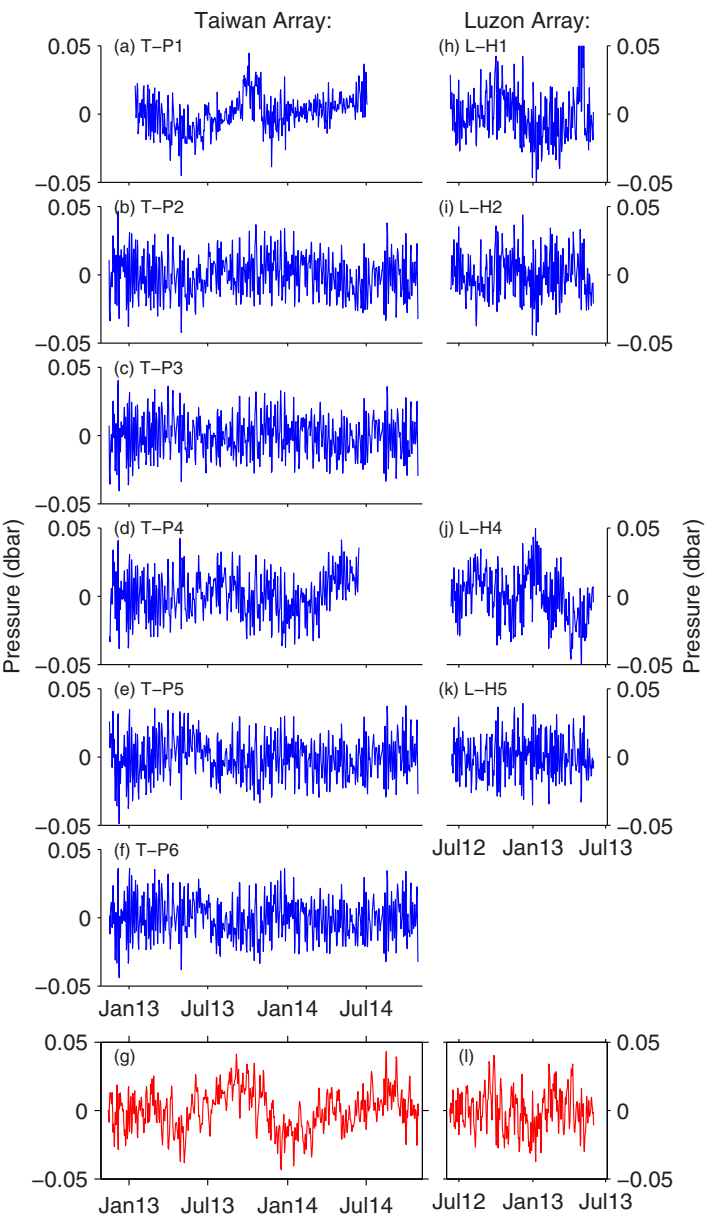

Figure A2. Three day low-pass filtered bottom pressure records from the PIESs (a–f) east of Taiwan and (h–k) northeast of Luzon, showing detided pressure records with the time means removed, a pressure-sensor drift [*Watts and Kontoyiannis*, 1990] removed for each instrument and a basin mode removed for each array. The respective basin modes for each region are shown in Figures A2g and A2l.

Appendix B: Taiwan-Array Data Processing and Mapping

B1. Velocity

Velocity data collected by the upward-looking ADCPs east of Taiwan are rotated 16° clockwise, which comprises a 4° rotation to account for the local magnetic declination and a 12° rotation so that the poleward (or "downstream") velocity is perpendicular to the line of instruments along the Yaeyama Ridge and the "cross-stream" velocity is positive offshore toward 102°. (The same rotations are applied to the velocities measured by the current sensor at site T-P4.) ADCP data are gridded onto a 10 km grid between 121.854°E, 23.841°N and 123.005°E, 23.608°N.

B2. Acoustic Travel Time

A τ_{1000} mean field $\bar{\tau}(x, y)$ for the region east of Taiwan is derived from 2149 hydrographic casts (from historical CTDs and Seaglider dives) acquired within the domain outlined in Figure 3 (black box). Within this domain, a mean field is calculated via *Barnes* [1964]

interpolation with empirically derived zonal and meridional smoothing length scales of 0.10° and 0.40°, respectively (as described in *Mensah et al.* [2016] for the Luzon array).

The processed hourly PIESs' τ_{1000} data are 3 day low-pass filtered and subsampled to 1 day interval. The daily time series of τ anomalies ($\tau_{1000} - \bar{\tau}$) are separated into low-passed and high-passed contributions using 39 days for the cutoff frequency. The low-passed time series are objectively mapped onto a 10 km grid with a correlation scale of 120 km and the high-passed time series with a correlation scale of 65 km. At site T-P1, τ data are missing or erroneous from the 356th sample. The missing data until the end of the time series (sample 717) are obtained by a least squares fitting whose coefficients b_0 and b_i are determined as follows:

$$y = b_0 + \sum_{i=1}^{i=6} b_i x_i + \varepsilon \tag{B1}$$

Here y is the time series of τ at site T-P1, x_1 to x_5 are the time series of τ at site T-P2 to T-P6, and x_6 is the time series of SSH anomaly data (from the gridded altimetry product) at the grid point located closest to T-P1; each time series spans the first to the 355th sample. The coefficients $b_0 \ldots b_6$ are the values that minimize the sum of the residuals ε. The time series of simulated τ at T-P1 τ^*_{P1} are obtained using these coefficients and the aforementioned time series. The fit between the simulated τ^*_{P1} and actual τ_{P1} between the first and 355th sample yields $r^2 = 0.59$.

At T-P4, τ data are missing from the 577th sample. The missing data until the end of the time series are obtained via the objective mapping inputting data from all the other PIES until sample 596, then inputting data at T-P2, T-P3, T-P5, and T-P6, thereafter.

As explained in section 3.1, two GEM lookup tables are used to interpret the Taiwan-array acoustic travel time data according to the method described in *Mensah et al.* [2016]. The reference level used for the GEMs here, 1000 dbar, is below the depth of the main thermocline, but shallow enough that a sufficient number of casts are available to build the lookup tables. A western GEM is used to convert τ_{1000} into specific volume anomaly (or density) profiles between 121.85°E and 122.05°E. An eastern GEM is used between 122.23°E and 123.00°E. The specific volume anomaly (or density) profiles at 122.14°E are obtained by linear interpolation of the values at 122.04°E and 122.23°E.

B3. Pressure

After removing a basin mode, which is common across the instruments in the Taiwan array (shown in Figure A2g with the basin mode for the Luzon array shown in Figure A2l), the pressure residuals from the PIESs east of Taiwan are split into low-passed and high-passed contributions [*Andres et al.*, 2008b; *Donohue et al.*, 2010] using 58 days for the cutoff frequency. These are objectively mapped onto a 10 km grid with low-pass field correlation scale of 70 km and a high-pass field correlation scale of 60 km. At site T-P1, pressure data are missing or erroneous from sample 1 to 62 and 596 to 717. The missing data are obtained via least square fit following (equation (B1)), this time by inputting data from all the other PIESs. The fit between actual and simulated pressure at T-P1 between samples 63 and 595 is $r^2 = 0.86$.

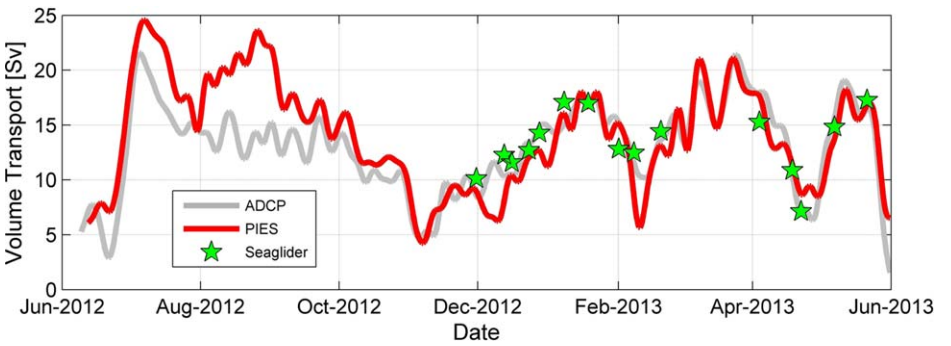

Figure C1. Comparison of transport northeast of Luzon calculated by different methods and platforms [after *Mensah et al.*, 2016]. Analogous to Figure 5 for the array east of Taiwan, the red curve is the PIES-derived absolute geostrophic transport and the gray curve is the ADCP-derived transport. Transports northeast of Luzon are 7 day low-pass filtered and span the surface to 600 dbar between 122.10°E and 122.87°E; the green stars are absolute geostrophic transports over the same area calculated from Seaglider transects [*Mensah et al.*, 2016].

Appendix C: Comparison of Luzon-Array Transports to Independent Estimates of Transport

Comparison between Taiwan-array transports and independent estimates is discussed in section 3.2. The comparison for the Luzon-array transports and independent estimates is detailed in *Mensah et al*. [2016] but is reviewed here briefly. The correspondence between leveled absolute geostrophic transports from PIESs (Figure C1, red line) and the total transports integrated between the ADCPs (gray line) is excellent with 3.0 Sv rms difference [*Mensah et al*., 2016] (Table 3). For this comparison, the endpoints for the transport integrations are between 122.10°E and 122.87°E and from the surface to 600 dbar. As noted in *Mensah et al*. [2016], the largest discrepancies between the ADCP-derived transports and the PIES-derived transports occur during two events in July 2012 and August/September 2012 and may be due to ageostrophic contributions to the transport (which are included in the ADCP-derived transports, but not in the PIES-derived transports). Comparison between 15 Seaglider-derived transports northeast of Luzon and the concurrent PIES-derived transports (which are both measures of the geostrophic absolute transport) give a 1.8 Sv rms difference [*Mensah et al*., 2016] (Table 3 and Figure C1, green stars).

Acknowledgments

M.A. was supported by Office of Naval Research (ONR) grants N00014-15-12593 and N00014-16-13069. S.J. was supported by Taiwan's Ministry of Science and Technology grants NSC 101-2611-M-002-018-MY3, MOST 103-2611-M-002-011, and MOST 105-2119-M-002-042. C.M.L. and B.M. were supported by ONR grant N00014-10-1-0308. T.B.S. was supported by ONR grant N00015-10-1-0469. The altimeter data used here are produced by Ssalto/Duacs and distributed by Aviso, with support from CNES (http://www.aviso.oceanobs.com/duacs/). The wind stress reanalysis data are provided by the National Centers for Environmental Prediction-National Center for Atmospheric Research (NCEP-NCAR).

References

Anderson, D. T. L., and A. E. Gill (1975), Spin-up of a stratified ocean, with applications to upwelling, *Deep Sea Res. Oceanogr. Abstr.*, *22*, 583–596.

Andres, M., M. Wimbush, J.-H. Park, K. L. Tracey, D. R. Watts, W. Teague, D. A. Mitchell, and H. Ichikawa (2005), East China Sea Kuroshio 2002–2004 data report, *GSO Tech. Rep. 2005-02*, The University of Rhode Island Graduate School of Oceanography.

Andres, M., J.-H. Park, M. Wimbush, X.-H. Zhu, K.-I. Chang, and H. Ichikawa (2008a), Study of the Ryukyu Current-Kuroshio system based on the integrated use of satellite altimetry and in situ data, *J. Oceanogr.*, *64*, 937–950.

Andres, M., M. Wimbush, J.-H. Park, K.-I. Chang, B.-H. Lim, D. R. Watts, H. Ichikawa, and W. J. Teague (2008b), Observations of Kuroshio flow variations in the East China Sea, *J. Geophys. Res.*, *113*, C05013, doi:10.1029/2007JC004200.

Andres, M., Y.-O. Kwon, and J. Yang (2011), Observations of the Kuroshio's barotropic and baroclinic responses to basin-wide wind forcing, *J. Geophys. Res.*, *116*, C04011, doi:10.1029/2010JC006863.

Andres, M., J. Yang, and Y.-O. Kwon (2012), Adjustment of a wind-driven two-layer system with mid-basin topography, *J. Mar. Res.*, *70*(6), 851–882.

Andres, M., S. Jan, T. B. Sanford, V. Mensah, L. Centurioni, and J. W. Book (2015), Mean structure and variability of the Kuroshio from northeastern Taiwan to southwestern Japan, *Oceanography*, *28*(4), 84–95, The University of Rhode Island Graduate School of Oceanography, doi:10.5670/oceanog.2015.84.

Baker-Yeboah, S., D. R. Watts, and D. Byrne (2009), Measurements of sea surface height variability in the eastern South Atlantic from pressure-sensor equipped inverted echo sounders: Baroclinic and barotropic components, *J. Atmos. Oceanic Technol.*, *26*(12), 2593–2609, doi:10.1175/2009JTECHO659.1.

Barnes, S. L. (1964), A technique for maximizing details in numerical weather-map analysis, *J. Appl. Meteorol.*, *3*(4), 396–409.

Beal, L. M., S. Elipot, A. Houk, and G. M. Leber (2015), Capturing the transport variability of a western boundary jet: Results from the Agulhas Current Time-Series Experiment (ACT), *J. Phys. Oceanogr.*, *45*, 1302–1324, doi:10.1175/JPO-D-14-0119.1.

Book, J. W., M. Wimbush, S. Imawaki, H. Ichikawa, H. Uchida, and H. Kinoshita (2002), Kuroshio temporal and spatial variations South of Japan determined from inverted echo sounder measurements, *J. Geophys. Res.*, *107*(C9), 3121, doi:10.1029/2001JC000795.

Chelton, D. B., M. G. Schlax, R. M. Samelson, and R. A. de Szoeke (2007), Global observations of large oceanic eddies, *Geophys. Res. Lett.*, *34*, L15606, doi:10.1029/2007GL030812.

Chen, C.-C., S. Jan, T.-H. Kuo, and S.-Y. Li (2017), Nutrient flux and transport in the upper ocean of the Kuroshio east of Taiwan, *J. Mar. Syst.*, *167*, 43–54, doi:10.1016/j.jmarsys.2016.11.004.

Donohue, K. A., D. R. Watts, K. Tracey, A. D. Greene, and M. Kennelly (2010), Mapping circulation in the Kuroshio Extension with an array of current and pressure recording inverted echo sounders, *J. Atmos. Oceanic Technol.*, *27*, 507–527, doi:10.1175/2009JTECHO686.1.

Gordon, A. L., P. Flament, C. Villanoy, and L. Centurioni (2014), The nascent Kuroshio of Lamon Bay, *J. Geophys. Res. Oceans*, *119*, 4251–4263, doi:10.1002/2014JC009882.

Ichikawa, H., H. Nakamura, A. Nishina, and M. Higashi (2004), Variability of north-eastward current southeast of northern Ryukyu Islands, *J. Oceanogr.*, *60*, 351–363.

Jan, S., Y. J. Yang, J. Wang, V. Mensah, T.-H. Kuo, M.-D. Chiou, C.-S. Chern, M.-H. Chang, and H. Chien (2015), Large variability of the Kuroshio at 23.75°N east of Taiwan, *J. Geophys. Res. Oceans*, *120*, 1825–1840, doi:10.1002/2014JC010614.

Johns, W. E., T. N. Lee, D. Zhang, R. Zantopp, C.-T. Liu, and Y. Yang (2001), The Kuroshio east of Taiwan: Moored transport observations from the WOCE PCM-1 array, *J. Phys. Oceanogr.*, *31*, 1031–1053.

Kalnay, E., et al. (1996), The NCEP/NCAR reanalysis 40-year project, *Bull. Am. Meteorol. Soc.*, *77*, 437–471, doi:10.1175/1520-0477(1996)077<0437:TNYRP>2.0.CO;2.

Kennelly, M., K. L. Tracey, and D. R. Watts (2007), Inverted Echo Sounder Data Processing Manual, *GSO Tech. Rep. 2007-02*.

Lee, C. M. (2015), Kuroshio transport and watermass modification in the vicinity of Luzon Strait, paper presented at 18th Pacific-Asian Marginal Seas Meeting, Naha, Japan, 21–23 April. [Available at https://global.riam.kyushu-u.ac.jp/pams/wp-content/uploads/2015/04/ABSTRACTS.pdf.]

Lien, R.-C., B. Ma, Y.-H. Cheng, C.-R. Ho, B. Qiu, C. M. Lee, and M.-H. Chang (2014), Modulation of Kuroshio transport by mesoscale eddies at the Luzon Strait entrance, *J. Geophys. Res. Oceans*, *119*, 2129–2142, doi:10.1002/2013JC009548.

Lien, R.-C., et al. (2015), The Kuroshio and Luzon Undercurrent east of Luzon Island, *Oceanography*, *28*(4), 54–63, doi:10.5670/oceanog.2015.81.

Meinen, C. S., and D. R. Watts (2000), Vertical structure and transport on a transect across the North Atlantic Current near 428°N: Time series and mean, *J. Geophys. Res.*, *105*, 21,869–21,891.

Mensah, V., S. Jan, M.-D. Chiou, T.-H. Kuo, and R.-C. Lien (2014), Evolution of the Kuroshio Tropical Water from the Luzon Strait to the east of Taiwan, *Deep Sea Res., Part I*, *86*, 68–81, doi:10.1016/j.dsr.2014.01.005.

Mensah, V., M. Andres, R.-C. Lien, B. Ma, C. Lee, and S. Jan (2016), Combining observations from multiple platforms across the Kuroshio northeast of Luzon: A highlight on PIES data, *J. Atmos. Oceanic Technol.*, *33*, 2185–2203, doi:10.1175/JTECH-D-16-0095.1.

Nitani, H. (1972), Beginning of the Kuroshio, in *Kuroshio, Its Physical Aspects*, edited by H. Stommel and K. Yoshida, pp. 129–163, Univ. of Tokyo Press.

Qiu, B., and S. Chen (2010), Interannual-to-decadal variability in the bifurcation of the North Equatorial Current off the Philippines, *J. Phys. Oceanogr.*, *40*, 2525–2538.

Rudnick, D. L., S. Jan, and C. M. Lee (2015), A new look at circulation in the western North Pacific, *Oceanography*, *28*(4), 16–23, doi:10.5670/oceanog.2015.77.

Sanford, T. B. (1971), Motionally induced electric and magnetic fields in the sea, *J. Geophys. Res.*, *76*, 3476–3492, doi:10.1029/JC076i015p03476.

Soeyanto, E., X. Guo, J. Ono, and Y. Miyazawa (2014), Interannual variations of Kuroshio transport in the East China Sea and its relation to the Pacific Decadal Oscillation and mesoscale eddies, *J. Geophys. Res. Oceans*, *119*, 3595–3616, doi:10.1002/2013JC009529.

Stommel, H. (1948), The westward intensification of wind-driven ocean currents, *Trans. AGU*, *29*(2), 202–206, doi:10.1029/TR029i002p00202.

Sun, C., and D. R. Watts (2001), A circumpolar gravest empirical mode for Southern Ocean hydrography, *J. Geophys. Res.*, *106*, 2833–2855, doi:10.1029/2000JC900112.

Sverdrup, H. (1947), Wind-driven currents in a baroclinic ocean; with application to the equatorial currents of the eastern Pacific, *Proc. Natl. Acad. Sci. U. S. A.*, *33*, 318–326.

Szuts, Z. B. (2012), Using motionally-induced electric signals to indirectly measure ocean velocity: Instrumental and theoretical developments, *Prog. Oceanogr.*, *96*(1), 108–127, doi:10.1016/j.pocean.2011.11.014.

Tsai, C.-J., M. Andres, S. Jan, V. Mensah, T. B. Sanford, R.-C. Lien, and C. M. Lee (2015), Eddy-Kuroshio interaction processes revealed by mooring observations off Taiwan and Luzon, *Geophys. Res. Lett.*, *42*, 8098–8105, doi:10.1002/2015GL065814.

Veronis, G., and H. Stommel (1956), The action of variable wind stresses on a stratified ocean, *J. Mar. Res.*, *15*, 43–75.

Vélez-Belchí, P., L. R. Centurioni, D.-K. Lee, S. Jan, and P. P. Niiler (2013), Eddy induced Kuroshio intrusions onto the continental shelf of the East China Sea, *J. Mar Res.*, *71*, 83–108, doi:10.1357/002224013807343470.

Watts, D. R., and H. Kontoyiannis (1990), Deep-ocean bottom pressure measurement: Drift removal and performance, *J. Atmos. Oceanic Technol.*, *7*, 296–306.

Watts, D. R., C. Sun, and S. Rintoul (2001), Two-dimensional gravest empirical modes determined form hydrographic observations in the Subantarctic Front, *J. Phys. Oceanogr.*, *31*, 2186–2209.

Yang, K.-C., J. Wang, C. M. Lee, B. Ma, R.-C. Lien, S. Jan, Y. J. Yang, and M.-H. Chang (2015), Two mechanisms cause dual velocity maxima in the Kuroshio east of Taiwan, *Oceanography*, *28*(4), 64–73, doi:10.5670/oceanog.2015.82.

Yang, Y., C.-T. Liu, J.-H. Hu, and M. Koga (1999), Taiwan Current (Kuroshio) and impinging eddies, *J. Oceanogr.*, *55*, 609–617.

Yang, Y. J., et al. (2015), Mean structure and fluctuations of the Kuroshio East of Taiwan from in situ and remote observations, *Oceanography*, *28*(4), 74–83, doi:10.5670/oceanog.2015.83.

Zhang, D., T. N. Lee, W. E. Johns, C. T. Liu, and R. Zantopp (2001), The Kuroshio east of Taiwan: Modes of variability and relationship to interior ocean mesoscale eddies, *J. Phys. Oceanogr.*, *31*, 1054–1074.

Zhu, X.-H., I.-S. Han, J.-H. Park, H. Ichikawa, K. Murakami, A. Kaneko, and A. Ostrovskii (2003), The northeastward current southeast of Okinawa Island observed during November 2000 to August 2001, *Geophys. Res. Lett.*, *30*(2), 1071, doi:10.1029/2002GL015867.